Biochemical Journal (2019) **476** 2521–2543
https://doi.org/10.1042/BCJ20190383

PORTLAND PRESS

Research Article

Structural and functional characterisation of human RNA helicase DHX8 provides insights into the mechanism of RNA-stimulated ADP release

Catarina Felisberto-Rodrigues[1,2,*], Jemima C. Thomas[1,*], Craig McAndrew[1], Yann-Vaï Le Bihan[1,2], Rosemary Burke[1], Paul Workman[1] and Rob L. M. van Montfort[1,2]

[1]Cancer Research UK Cancer Therapeutics Unit, Division of Cancer Therapeutics, The Institute of Cancer Research, London SM2 5NG, U.K.; [2]Division of Structural Biology, The Institute of Cancer Research, London SW3 6JB, U.K.

Correspondence: Rob L. M. van Montfort (rob.vanmontfort@icr.ac.uk)

DHX8 is a crucial DEAH-box RNA helicase involved in splicing and required for the release of mature mRNA from the spliceosome. Here, we report the biochemical characterisation of full-length human DHX8 and the catalytically active helicase core DHX8Δ547, alongside crystal structures of DHX8Δ547 bound to ADP and a structure of DHX8Δ547 bound to poly(A)$_6$ single-strand RNA. Our results reveal that DHX8 has an *in vitro* binding preference for adenine-rich RNA and that RNA binding triggers the release of ADP through significant conformational flexibility in the conserved DEAH-, P-loop and hook-turn motifs. We demonstrate the importance of R620 and both the hook-turn and hook-loop regions for DHX8 helicase activity and propose that the hook-turn acts as a gatekeeper to regulate the directional movement of the 3′ end of RNA through the RNA-binding channel. This study provides an in-depth understanding of the activity of DHX8 and contributes insights into the RNA-unwinding mechanisms of the DEAH-box helicase family.

Introduction

The splicing of pre-mRNA to remove non-coding introns is a crucial process in gene expression in all eukaryotes [1]. It is estimated that ∼95% of human genes are alternatively spliced through differences in the way exons are joined [2], thus greatly increasing the complexity of the proteome by producing multiple mature mRNA transcripts from the same gene [2]. Under normal conditions, alternative splicing is tightly regulated, but changes in alternative splicing are increasingly linked to a variety of human diseases, and in particular to cancer [3–5].

Splicing is catalysed by the spliceosome, a large and dynamic protein–RNA complex consisting of five small nuclear ribonucleoproteins (snRNPs) and, in humans, ∼200 accessory proteins [6]. The snRNPs are crucial in the recognition of the splice sites and bind in a well-defined order to assemble the spliceosome on the pre-mRNA substrate. Major conformational changes are required to enable the two distinct catalytic splicing reactions, and for the subsequent release of the mature mRNA [7]. These extensive conformational changes are mediated by at least eight nucleotide triphosphate (NTP)-dependent RNA helicases belonging to the helicase superfamily 2 (SF2) [8,9]. One of these is the DEAH/RHA RNA helicase DHX8, which is required for the release of mature mRNA from the spliceosome [10,11]. In addition, its functional homologue in yeast (Prp22) plays a crucial role in splicing fidelity and proof-reading mechanisms by promoting optimal and rejecting suboptimal 3′ splice sites [12,13]. This allows the sampling of different sites, indicating a role in the activation of alternative splicing mechanisms [14,15]. Mutations of DHX8 in zebrafish and siRNA silencing of DHX8 in human HeLa cells lead to incomplete mRNA splicing and defects in cell division, further emphasising its critical role in splicing and suggesting that DHX8 is also required for mitotic exit [16].

*These authors contributed equally to this work.

Received: 21 May 2019
Revised: 9 August 2019
Accepted: 12 August 2019

Accepted Manuscript online: 13 August 2019
Version of Record published: 14 September 2019

PORTLAND PRESS

Biochemical Journal (2019) **476** 2521–2543
https://doi.org/10.1042/BCJ20190383

Similar to other DEAH-box RNA helicases, DHX8 is composed of a highly variable N-terminal domain, and a conserved C-terminal helicase domain. The latter contains two RecA domains, RecA1 and RecA2, that form the helicase core and contain up to 12 characteristic motifs that participate in ATP binding and hydrolysis, RNA binding and helicase activity [17]. In addition to the RecA domains, the DHX8 helicase domain contains C-terminally located winged-helix (WH), ratchet-like and oligonucleotide binding (OB)-fold domains [17,18].

While the yeast spliceosomal DEAH-box helicases have been widely studied, with ATPase and RNA-unwinding analyses reported for Prp22, Prp2, Prp16 and Prp43 [19–24], none of their human homologues have been characterised biochemically. Similarly, crystal structures have been published for the helicase domains of Prp43 from *Saccharomyces cerevisiae* (scPrp43) and *Chaetomium thermophilum* (ctPrp43) in complex with ADP or ATP mimetics, and bound to poly(U) RNA substrates [25–28], providing valuable insights into nucleotide binding and the RNA-unwinding mechanism of this helicase. However, only one ADP-bound structure is available of its human homologue DHX15 [29].

Insights into the spliceosomal location and orientation of Prp22 and DHX8 have been obtained from cryo-electron microscopy structures of different states of the yeast and human spliceosomes [30–33], but due to the peripheral location of DHX8/Prp22 in the spliceosome, this information is mostly of only moderate resolution. In addition, the structure of the DHX8 N-terminal S1 RNA binding domain has been solved by NMR (PDB ID: 2EQS), and the crystal structure of part of the helicase core comprising the C-terminal WH, ratchet-like and OB-fold domains has been reported [34]. A recent publication describing crystal structures of apo and poly(U)-bound *Chaetomium thermophilum* Prp22 (ctPrp22) has provided high-resolution structural information for this homologue [35]. However, given the importance of alternative splicing in human diseases, and the recognition that helicases constitute a class of underexploited druggable therapeutic cancer targets [36,37], it is vitally important that the structure and function of the human DEAH-box helicases are characterised in detail, and that the differences between their homologues and those from other species are well understood.

Here, we describe the recombinant generation and biochemical characterisation of full-length human DHX8 (fl-DHX8) and a truncated construct containing the complete catalytically active C-terminal helicase core region (DHX8Δ547). We also report the crystal structures of DHX8Δ547 bound to ADP and of DHX8Δ547 bound to a single-stranded poly-adenine RNA substrate (poly(A)$_6$). We confirm for the first time that human DHX8 hydrolyses ATP and can separate nucleic acid duplexes *in vitro*, and we show that the minimal RNA substrate required for binding has a length of four nucleotides. We find that DHX8 makes base-specific contacts with RNA and preferentially binds adenine-rich RNA *in vitro*. Our RNA-bound DHX8Δ547-A$_6$ structure represents a state in the RNA translocation mechanism immediately following ADP release and shows extensive flexibility in the conserved DEAH motif and P-loop, which may facilitate nucleotide release. Compared with other helicase structures, DHX8Δ547-A$_6$ reveals unexpected differences in the interactions between the RNA substrate and the DEAH-specific hook-turn motif. We demonstrate that RNA binding triggers nucleotide release and establish the importance of R620 and both the hook-loop and hook-turn for DHX8 helicase activity, proposing that the hook-turn acts as a gatekeeper to aid correct directional RNA movement through the RNA-binding tunnel. The combination of our biochemical and structural data offers a detailed characterisation of human DHX8 and contributes significantly to the understanding of the RNA-unwinding mechanism of the DEAH-box helicase family.

Materials and methods

Cloning and mutagenesis

All DHX8 constructs were generated by PCR cloning using restriction enzymes. The template for amplification was kindly provided by Emmanuel De Billy (encoding protein corresponding to UniProt Q14562). To generate His$_6$GST-DHX8Δ547, the coding sequence for residues A548 to R1220 was inserted into a version of pFastBac™ 1 (Thermo Fisher Scientific, Waltham, U.S.A.), modified to encode an N-terminal His$_6$GST-tag followed by an HRV 3C protease cleavage site. Both vector and insert were digested with NdeI and EcoRI restriction enzymes. To generate full-length DHX8 (fl-DHX8-His$_6$) and DHX8Δ547-His$_6$, PCR primers were designed, so that a His$_6$-tag would be fused to the C-terminus of DHX8. The resultant PCR amplicons encoding fl-DHX8 (M1 to R1220) or DHX8Δ547 (A548 to R1220) were inserted into the pFBDM vector (Geneva Biotech, Geneva, Switzerland) downstream of the polyhedrin promoter. Both vector and insert were digested with BamHI and NotI restriction enzymes. DHX8Δ547-His$_6$ mutants were generated by site-directed mutagenesis using a QuikChange (Agilent, Santa Clara, U.S.A.) protocol.

Biochemical Journal (2019) 476 2521–2543
https://doi.org/10.1042/BCJ20190383

Protein expression and purification

Viruses were prepared using the Bac-to-Bac® Baculovirus Expression System (Thermo Fisher Scientific). His_6GST-DHX8Δ547 was expressed in High Five™ cells (Thermo Fisher Scientific) while fl-DHX8-His_6, DHX8Δ547-His_6 and DHX8Δ547-His_6 mutants were expressed in Sf9 cells (Thermo Fisher Scientific). Both cell lines were grown in shaker flasks containing Insect-XPRESS media (Lonza, Basel, Switzerland) with 30 μg/ml penicillin and 50 μg/ml streptomycin at 27°C, 140 rpm to a cell density of $\sim 2 \times 10^6$/ml. Cultures were subsequently infected with sufficient virus to cause cessation of cell growth within 24 h. Infected cultures were harvested ∼48 h post-infection and the cell pellets stored at −80°C.

Wild-type His_6GST-DHX8Δ547, fl-DHX8-His_6, DHX8Δ547-His_6 as well as DHX8Δ547-His_6 point mutant proteins were purified using the following procedures, all performed at 4°C. Cell pellets were thawed and resuspended in 100 ml lysis buffer [50 mM HEPES (pH 7.4), 500 mM NaCl, 10% (*v*/*v*) glycerol] containing 1× complete EDTA-free protease inhibitor tablet (Roche, Welwyn Garden City, U.K.) and 1:2000 Benzonase (Millipore Ltd, Hertfordshire, U.K.). Cells were lysed by sonication and insoluble material was removed by centrifugation using a Beckman JA-25.50 rotor for 1 h at 21 000 rpm, and the supernatant filtered. His_6GST-DHX8Δ547 lysate was loaded onto a 5 ml GSTrap fast-flow column (GE Healthcare, Buckinghamshire, U.K.) and the column was washed with lysis buffer, followed by a high salt wash [50 mM HEPES (pH 7.4), 2 M NaCl]. Protein was eluted using 20 mM reduced glutathione in lysis buffer and the His_6GST-tag was cleaved by the addition of HRV 3C protease (Thermo Fisher Scientific).

DHX8 lysates containing a C-terminal His_6-tag were loaded onto 2 × 5 ml HisTrap fast-flow columns (GE Healthcare) and the column was washed with lysis buffer containing 25 mM imidazole, followed by a high salt wash [50 mM HEPES (pH 7.4), 2 M NaCl]. Protein was eluted using a gradient of 25–500 mM imidazole in lysis buffer.

Eluted fractions were analysed by SDS–PAGE and DHX8-containing fractions were pooled for heparin purification on a 5 ml HiTrap Heparin HP column (GE Healthcare), followed by gel filtration using a HiLoad Superdex 200 16/60 column (GE Healthcare). The gel filtration column was equilibrated with protein storage buffer comprising 50 mM HEPES (pH 7.4), 150 mM NaCl, 10% (*v*/*v*) glycerol, 0.5 mM TCEP. Protein yields were ∼0.5 mg/l for His_6GST-DHX8Δ547, 1 mg/l for fl-DHX8-His_6 and 5 mg/l for DHX8Δ547-His_6 and the mutants.

Gel-based unwinding assay

The gel-based unwinding assay is based on a published Prp22 unwinding assay [20] and uses an RNA/DNA duplex substrate comprising a 60-mer RNA strand (RNA60) annealed to a 30-mer DNA strand fluorescently labelled on the 3′ end (DNA30-ATTO680). The assay also includes a 30-mer DNA strand (cDNA30) with a sequence complementary to the labelled DNA30 to capture this probe when released from the RNA/DNA duplex. The RNA/DNA duplex was chosen as the optimal assay substrate because it was found to be best to observe *in vitro* duplex disruption when compared with more stable RNA/RNA duplexes.

The single-strand RNA60 oligomer was purchased from Dharmacon (Colorado, U.S.A.) using the sequence reported for Prp22 [20]. The fluorescently labelled DNA probe and cDNA30 were purchased from Eurofins Genomics (Ebersberg, Germany). The RNA60 sequence was 5′-GGGCGAAUUGGGCCCUCUAGAUGCAUG CUCGAGCGGCCGCCAGUGUGAUGGAUAUCUGCA-3′, the DNA30-ATTO680 sequence 5′-GAGCATGCA ATCTAGAGGGCCCAATTCGCCC-3′ and the cDNA30 sequence 5′-GGGCGAATTGGGCCCTCTAGATGCA TGCTC-3′.

The RNA/DNA duplex was formed by heating a 2:1 ratio of RNA60:DNA30-ATTO680 at 95°C for 5 min, followed by slow cooling to room temperature. Reaction mixtures with a total volume of 20 μl and containing 10 nM RNA/DNA duplex, 100 nM cDNA30 and 10, 20, 50, 100, 200 and 500 nM DHX8 were incubated at 37°C for 1 h in 40 mM Bis–Tris (pH 6.5), 2 mM ATP, 2 mM $MgCl_2$, 2 mM DTT and 0.05 mg/ml BSA. Reactions were stopped by the addition of 20 μl loading buffer consisting of 0.4% SDS (*w*/*v*), 20 mM EDTA, 2 mM DTT, 8% (*v*/*v*) glycerol, 0.1% (*w*/*v*) Orange G, 400 μg/ml Proteinase K and incubation at 37°C for a further 1 h. Subsequently, 25 μl of each sample was analysed on a 10% (*v*/*v*) polyacrylamide native gel and imaged using a LI-COR Odyssey Fc imaging system (LI-COR Biosciences, Cambridge, U.K.).

ATPase assays

All ATPase assays were performed using the ADP Glo Max assay system (Promega, Southampton, U.K.) in white 384-well OptiPlates (PerkinElmer, Buckinghamshire, U.K.). The luminescence signal was read on an EnVision multimode plate reader (PerkinElmer).

Biochemical Journal (2019) 476 2521–2543
https://doi.org/10.1042/BCJ20190383

Each well contained a total volume of 20 μl made up of 5 μl ATPase reaction components, 5 μl ADP Glo Reagent, 10 μl ADP Glo Max Detection reagent. The ATPase reaction consisted of 200 nM fl-DHX8-His_6 or DHX8Δ547-His_6 with doubling dilutions of ATP to a maximum concentration of 2 mM, ± 20 μM poly$(A)_{10}$ ssRNA. Preliminary assay development experiments confirmed that the generation of ADP is linear up to 45 min. Thus, the assay was incubated for 45 min at room temperature in an assay buffer consisting of 50 mM HEPES (pH 7.4), 150 mM NaCl, 20 mM $MgCl_2$, 1 mM TCEP, 0.1% (*w/v*) CHAPS, 2% (*v/v*) DMSO, before the reaction was stopped by the addition of the ADP Glo Reagent. ATP/ADP standards were included in each plate to convert the luminescence signal to ADP concentration. Data were fitted to Michaelis–Menten kinetics using GraphPad Prism (GraphPad Prism version 7.00 for Windows, GraphPad Software, La Jolla, CA, U.S.A., www.graphpad.com).

Fluorescence anisotropy assays

All steady-state fluorescence anisotropy (FA) assays [38] were performed in total well volumes of 10 μl using black 384-well ProxiPlates (PerkinElmer). Assays were sealed and incubated at room temperature for 2 h to allow the system to reach equilibrium and the signal to stabilise before the fluorescent signal was measured on an EnVision multimode plate reader (PerkinElmer). Assay optimisation confirmed that the protein was stable for over 3 h under the final conditions.

ATP binding was assessed using 10 nM of an N6-(6-aminohexyl)-ATTO488-ATP probe (ATTO488-ATP, Jena Bioscience, Jena, Germany) in 50 mM HEPES (pH 7.4), 150 mM NaCl, 2 mM $MgCl_2$, 1 mM TCEP, 0.1% (*w/v*) CHAPS, 2% (*v/v*) DMSO. Data were fitted to a quadratic binding model [39] using GraphPad Prism. Competition FA experiments with ATTO488-ATP used 10 nM ATTO488-ATP, 500 nM fl-DHX8-His_6 or DHX8Δ547-His_6 and doubling dilutions of the competitor nucleotide (maximum concentration 100 μM).

RNA binding was assessed using 5 nM of a 5′-labelled Cy5-poly$(A)_{10}$ ssRNA probe (Dharmacon) in an assay buffer containing 50 mM HEPES (pH 7.4), 150 mM NaCl, 2 mM $MgCl_2$, 1 mM TCEP, 0.1% (*w/v*) CHAPS, 2% (*v/v*) DMSO ± 2 mM nucleotide. Data were fitted to a quadratic binding model using GraphPad Prism. Competition FA experiments with Cy5-poly$(A)_{10}$ used 5 nM Cy5-poly$(A)_{10}$, 50 nM fl-DHX8-His_6 or DHX8Δ547-His_6 and doubling dilutions of competitor RNA (Dharmacon) with a maximum concentration of 12.5 μM. The buffer for Cy5-poly$(A)_{10}$ competition assays included 2 mM ADP-AlF_x.

Thermal shift assays

Thermal shift assays were performed in total well volumes of 5 μl using FrameStar 384-well PCR plates (4titude, Surrey, U.K.). The fluorescent signal was measured on a C1000 Thermal Cycler CFX384 Real-Time System (Bio-Rad, Hertfordshire, U.K.). Each well contained 5 μM protein and 10× Sypro Orange dye (Sigma–Aldrich, Dorset, U.K.) in 50 mM HEPES (pH 7.4), 150 mM NaCl, 2 mM $MgCl_2$, 1 mM TCEP and 2% DMSO. Data were plotted using GraphPad Prism.

Crystallisation and structure determination

Crystallisation trials were performed with protein obtained from the His_6GST-DHX8Δ547 construct. DHX8Δ547 crystals were grown in the presence of ADP at 18°C using the hanging-drop vapour-diffusion method. The crystallisation drops were composed of 0.5 μl protein solution, consisting of 3 mg/ml DHX8Δ547, 1 mM ADP and 1 mM $MgCl_2$, and 1.5 μl reservoir solution comprising 15% (*v/v*) 2-Methyl-2,4-pentanediol (MPD), 100 mM Sodium Acetate pH 5.5 and 6% (*v/v*) DMSO, and placed over 250 μl reservoir solution. Crystals were cryo-protected prior to data collection by supplementing the mother-liquor with 30% (*v/v*) ethylene glycol and flash frozen in liquid nitrogen.

For the elucidation of the ADP-bound DHX8Δ547 structure, X-ray data to 2.6 Å resolution were collected at the ID23.1 beamline at the European Synchrotron Radiation Facility (ESRF), Grenoble, France. The crystal belonged to the space group $P2_1$ with four independent DHX8 molecules in the asymmetric unit. Data were integrated with DIALS [40] and scaled and merged with AIMLESS [41]. The data were processed using $CC_{1/2}$ and completeness as cut-off criteria [42]. The DHX8Δ547-ADP structure was determined by molecular replacement using PHASER [43]. The RecA1 and RecA2 domains of *S. cerevisiae* Prp43 (PDB: 2XAU) and the helicase-associated domain of DHX8 (PDB: 3I4U) were used as two independent search models. The structure was refined using BUSTER [44], alternated with manual building rounds using COOT [45].

A second dataset from a DHX8Δ547-ADP crystal, also collected at beamline ID23.1 at the ESRF, allowed improvement of the structure to a resolution of 2.3 Å. This dataset was integrated using XDS and scaled and

Biochemical Journal (2019) 476 2521–2543
https://doi.org/10.1042/BCJ20190383

merged with AIMLESS. Molecular replacement was conducted using PHASER with the 2.6 Å DHX8Δ547 structure as search model. Refinement of the 2.3 Å structure was performed using the same procedure as outlined above.

For the DHX8Δ547 structure bound to poly(A)$_6$ RNA, a DHX8Δ547 crystal grown in the presence of ADP was soaked with 1 mM poly(A)$_6$ ssRNA at 4°C for 48 h. X-ray data to 3.2 Å resolution were collected at beamline ID30A-3 at the ESRF. The data were integrated using DIALS and were scaled and merged using AIMLESS. The crystal belonged to the space group $P2_12_12$ with two independent DHX8 molecules in the asymmetric unit. Molecular replacement was performed with PHASER using the 2.3 Å DHX8Δ547-ADP structure as search model. Subsequent refinement was carried out using iterative cycles of BUSTER and model building with COOT. As the space group of the crystals changed due to soaking of RNA, we confirmed the correct space group of the RNA-bound structure by processing the orthorhombic data in the monoclinic space group of the ADP-bound structures. This resulted in a significantly worse overall R_{meas} (54.5%) and further refinement using BUSTER did not converge. We also checked the space group of the ADP-bound structures by processing the monoclinic data in the higher symmetry orthorhombic space group of the RNA-bound structure which also resulted in worse statistics. The quality of all structures was assessed with MOLPROBITY [46]. All structural figures were generated with CHIMERA [47].

Results

DHX8 is an NTPase with RNA-unwinding capability

The biochemical characterisation of human DHX8 has not previously been reported. To enable this, we generated recombinant full-length DHX8 (fl-DHX8) and DHX8Δ547, a truncated construct consisting of the two RecA domains and the C-terminal WH, ratchet-like and OB-fold domains, but with the N-terminal region containing the RS and S1 domains removed (Figure 1A and Supplementary Figure S1).

DEAH-box helicases are characterised by their ability to unwind duplex nucleic acid substrates and typically separate substrates with a 3′ single-strand RNA overhang *in vitro* [48]. Analogous to an unwinding assay reported for yeast Prp22, we developed a fluorescent gel-based assay to investigate the unwinding activity of fl-DHX8 and DHX8Δ547, based on an RNA–DNA duplex with an RNA 3′ single-strand overhang of 30 bases. Both fl-DHX8 and DHX8Δ547 showed concentration and time-dependent separation of the RNA–DNA duplex (Figure 1B,C), implying that the N-terminal region is not essential for helicase activity. As has been observed for yeast Prp22, duplex separation was dependent on the presence of ATP (Figure 1D), but no additional protein cofactor was required [20,23,49].

To examine the ATPase activity of DHX8, we established an ADP Glo assay obeying Michaelis–Menten kinetics (Figure 2A and Table 1). K_m values for ATP were similar for fl-DHX8 (K_m = 39 μM) and DHX8Δ547 (K_m = 40 μM), but with a k_{cat} of 6.5 min^{-1} DHX8Δ547 had a higher ATP turnover rate compared with the full-length enzyme (k_{cat} = 1.7 min^{-1}), possibly indicating inhibitory modulation by the N-terminal region. Catalytic rates were increased in the presence of poly(A)$_{10}$ ssRNA for both DHX8Δ547 (k_{cat} = 18 min^{-1}) and fl-DHX8 (k_{cat} = 2.6 min^{-1}), demonstrating that DHX8 ATPase activity is stimulated by RNA.

Following the confirmation of DHX8 ATPase activity, we developed a steady-state FA assay to investigate nucleotide binding. Nucleotide-bound structures of other DEAH-box helicases show that while the bound nucleotide is mostly buried, its adenine 6-amino group is more solvent-exposed [28,50]. Therefore, we selected an available ATP probe labelled with the ATTO488 fluorophore attached via the adenine N6 position (N6-(6-aminohexyl)-ATTO488-ATP) (Supplementary Figure S2). Both fl-DHX8 and DHX8Δ547 bind the probe with nanomolar affinities (Figure 2B). However, given the inherent ATPase activity of DHX8 and the large excess of protein over probe, we recognise that ATTO488-ATP is rapidly hydrolysed during the assay and the K_d values reflect those for ATTO488-ADP. Similarly, unlabelled ATP added to displace the probe will have been hydrolysed before the assay reached equilibrium. This is supported by the IC_{50} values for ATP and the slowly hydrolysable ATP analogue ATPγS in the competition FA assay, which are very similar to that of ADP (2.8, 1.5 and 2.6 μM, respectively, Figure 2C). In contrast, adenine, adenosine and AMP could not displace ATTO488-ATP (Figure 2C), demonstrating the importance of the β-phosphate for nucleotide binding [51–53].

This FA assay was subsequently used to examine the ability of different nucleotides to bind in the ATP-binding site by displacing the probe (Figure 2D). Both fl-DHX8 and DHX8Δ547 preferentially bind the purine nucleotides ADP and GDP, but were also able to bind CDP, TDP and UDP, as has been reported for

Biochemical Journal (2019) 476 2521–2543
https://doi.org/10.1042/BCJ20190383

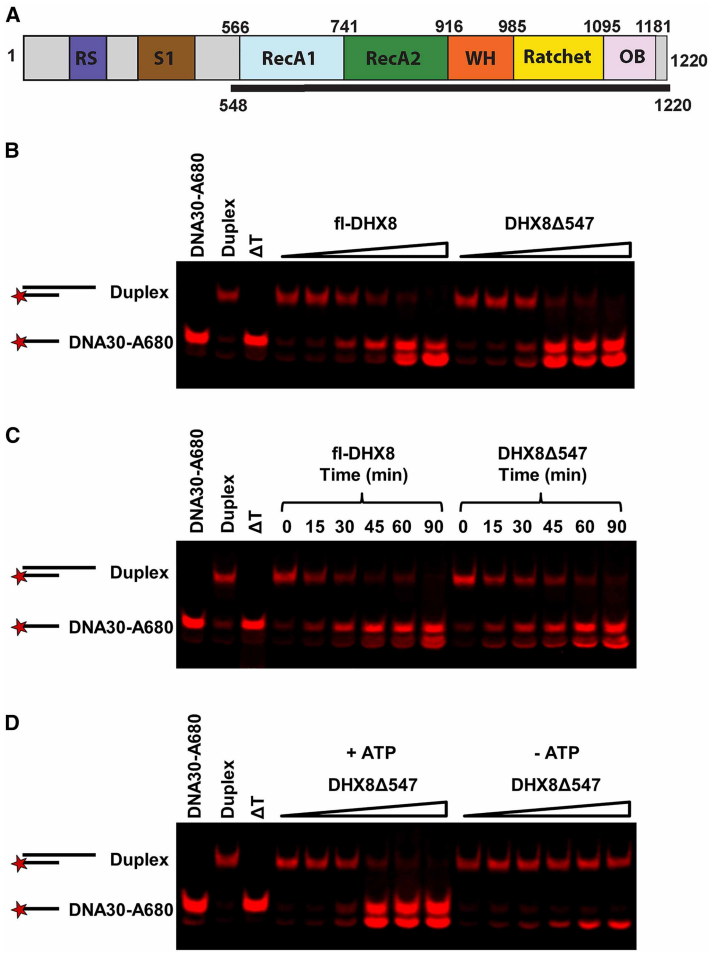

Figure 1. Characterisation of DHX8 nucleic acid unwinding activity.

(**A**) Domain organisation of DHX8 with domain boundaries indicated by numbers above. The bottom bar indicates N-terminally truncated DHX8Δ547. (**B**) An RNA/DNA duplex (10 nM) comprising a 60-mer RNA strand and 30-mer DNA strand fluorescently labelled on the 3′ end (DNA30-A680) was unwound in the presence of increasing concentrations of fl-DHX8 or DHX8Δ547 (10, 20, 50, 100, 200, 500 nM). (**C**) The RNA/DNA duplex was incubated with 100 nM fl-DHX8 or DHX8Δ547 and samples were monitored at the time points indicated, confirming that fl-DHX8 and DHX8Δ547 duplex separation is time-dependent. (**D**) The RNA/DNA duplex was incubated with increasing concentrations of DHX8Δ547 (10, 20, 50, 100, 200, 500 nM) in the presence or absence of 2 mM ATP. ATP was required for duplex separation. For all gels, *ΔT* shows the migration of DNA30-A680 after heating the duplex at 95°C for 5 min. Data are representative of three independent experiments. The DNA30-A680 probe migrates as two bands, possibly due to the presence of different conformations in the native gel. Therefore, the disappearance of the duplex band was used to monitor unwinding activity.

several other DEAH-box helicases [20,22,52,54]. Overall, the FA, ATPase and unwinding assays show that DHX8 behaves as a DEAH-box helicase, and does not require its N-terminal domains for enzymatic function.

In vitro RNA affinity is enhanced by ATP mimetics and highest for adenine-rich RNA

To gain insights into the effects of ATP hydrolysis on DHX8 RNA binding, we developed an FA assay with 5′-Cy5-labelled 10-mer polyA RNA (Cy5-poly(A)$_{10}$) as the probe. PolyA RNA was chosen to ensure that the RNA contained no secondary structure. DHX8 Cy5-poly(A)$_{10}$ binding affinities were determined in the presence of ATP mimetic ADP-BeF_3, the ATP transition state mimic ADP-AlF_x, ADP and in the absence of nucleotide (Figure 3A). In the presence of ATP mimetics ADP-BeF_3 and ADP-AlF_x, DHX8 has high affinity

Biochemical Journal (2019) **476** 2521–2543
https://doi.org/10.1042/BCJ20190383

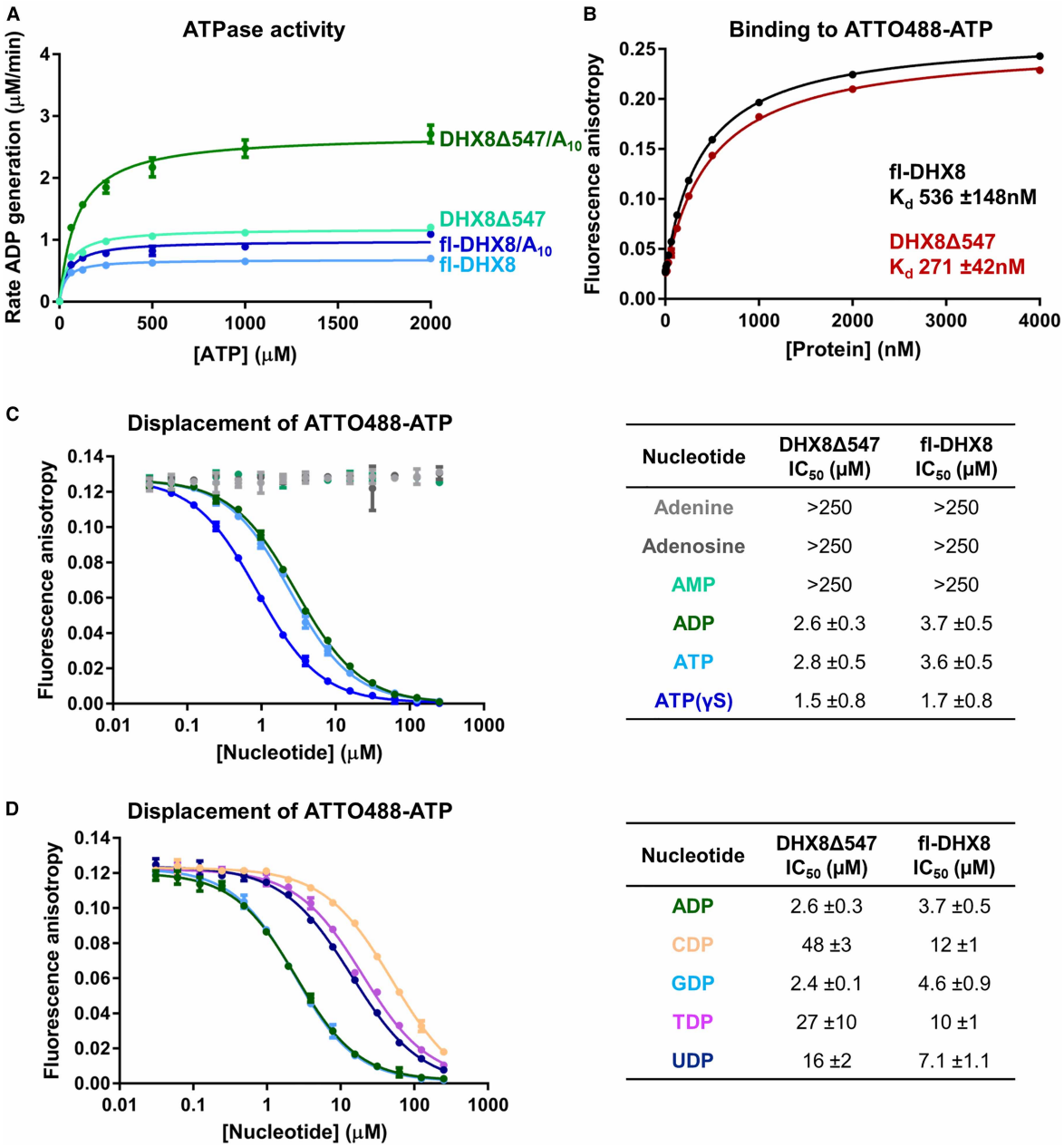

Nucleotide	DHX8Δ547 IC_{50} (μM)	fl-DHX8 IC_{50} (μM)
Adenine	>250	>250
Adenosine	>250	>250
AMP	>250	>250
ADP	2.6 ±0.3	3.7 ±0.5
ATP	2.8 ±0.5	3.6 ±0.5
ATP(γS)	1.5 ±0.8	1.7 ±0.8

Nucleotide	DHX8Δ547 IC_{50} (μM)	fl-DHX8 IC_{50} (μM)
ADP	2.6 ±0.3	3.7 ±0.5
CDP	48 ±3	12 ±1
GDP	2.4 ±0.1	4.6 ±0.9
TDP	27 ±10	10 ±1
UDP	16 ±2	7.1 ±1.1

Figure 2. Characterisation of DHX8 ATP binding and ATPase activity.

(**A**) ATPase activity of fl-DHX8 and DHX8Δ547 in the absence and presence of poly(A)$_{10}$ RNA. Data are fitted using the Michaelis–Menten model and kinetic parameters are shown in Table 1. (**B**) Titration of fl-DHX8 and DHX8Δ547 against the fluorescently labelled ATTO488-ATP probe. Data are fitted to a quadratic binding equation. (**C**) FA assay showing the displacement of ATTO488-ATP from DHX8Δ547 by ATP derivatives. Data points for adenine, adenosine and AMP are overlaid with each other. The calculated IC_{50} values are shown on the right-hand side. IC_{50} values >250 μM are too weak to be accurately determined. (**D**) FA assay showing the displacement of ATTO488-ATP from DHX8Δ547 by NDP nucleotides. Curves for ADP and GDP are overlaid with each other. The calculated IC_{50} values are shown on the right-hand side. ATTO488-ATP background fluorescence has been subtracted for all data points in (**C**) and (**D**). Graphs for fl-DHX8 are shown in Supplementary Figure S3A,B. ATTO488-ATP is hydrolysed before the experiment reaches equilibrium and therefore represents ATTO488-ADP. Graphical data are representative of at least two independent experiments. K_d and IC_{50} values are the averages from at least two independent experiments ± standard deviations.

Biochemical Journal (2019) 476 2521–2543
https://doi.org/10.1042/BCJ20190383

Table 1 Kinetic parameters for ATPase activity of DHX8 constructs with and without poly(A)$_{10}$ RNA

	No RNA		+ poly(A)$_{10}$ RNA	
	K_m (μM)	k_{cat} (min^{-1})	K_m (μM)	k_{cat} (min^{-1})
fl-DHX8	39 ± 9	1.7 ± 0.1	59 ± 14	2.6 ± 0.1
DHX8Δ547	40 ± 7	6.5 ± 1.1	121 ± 30	18 ± 5
DHX8Δ547-R620A	63 ± 25	10 ± 2	93 ± 26	14 ± 3
DHX8Δ547-HT	191 ± 46	35 ± 8	1184 ± 145	235 ± 39
DHX8Δ547-HL	117 ± 24	22 ± 4	125 ± 32	22 ± 3

K_m values are for ATP. Values are averages of three independent experiments ± standard deviations. For methods to derive kinetic constants, see the Materials and methods section.

for RNA with K_d values of ∼10 nM. However, the affinity for RNA is over 90-fold weaker in the absence of nucleotide and in the presence of ADP, the RNA affinity is too weak to determine. These results indicate that DHX8-mediated disruption of RNA interactions occurs through a series of alternating strong and weak RNA binding events controlled by ATP hydrolysis.

In general, SF2 helicases such as DHX8 are not believed to have RNA sequence specificity as they act on numerous different substrates. However, recently DEAH-box helicases demonstrating substrate preference have been reported. Examples include *Drosophila* DHX9 (also known as MLE), which preferentially binds uracil-rich RNA [50], and *Drosophila* DHX36, which has a preference for guanine-rich DNA [55]. To investigate whether DHX8 has any sequence specificity, we first confirmed that DHX8 is an RNA-specific helicase by showing that a poly(dA)$_{10}$ DNA strand could not displace Cy5-poly(A)$_{10}$ from DHX8 in the presence of ADP-AlF$_x$ (Figure 4A). The displacement of the probe with poly(A)$_{10}$, poly(C)$_{10}$, poly(G)$_{10}$ and poly(U)$_{10}$ RNA indicated that DHX8 has a preference for binding adenine-rich sequences as the rank order of IC$_{50}$ values was poly (A)$_{10}$<< poly(U)$_{10}$ < poly(C)$_{10}$< poly(G)$_{10}$ (Figure 4A). To confirm that the activity of poly(U)$_{10}$ was not due to sequestering of the probe, the direct binding of Cy5-poly(U)$_{10}$ to DHX8Δ547 in both the presence of ADP-AlF$_x$ and without a nucleotide was demonstrated (Figure 4B,C). In line with our competition assay, the K_d of Cy5-poly(U)$_{10}$ in the presence ADP-AlF$_x$ (K_d = 262 nM) was significantly weaker than that of Cy5-poly (A)$_{10}$, further implying that DHX8 has a preference for adenine-rich RNA sequences *in vitro*.

Subsequently, we determined the minimum RNA length required for binding to fl-DHX8 and DHX8Δ547. In the presence of ADP-AlF$_x$, poly(A) RNA strands consisting of 5–20 nucleotides all displaced the Cy5-poly (A)$_{10}$ probe with submicromolar IC$_{50}$ values (Figure 3B). However, the IC$_{50}$ of poly(A)$_4$ RNA is 12-fold weaker than that of poly(A)$_5$, and strands composed of three or two nucleotides do not displace the probe at all. IC$_{50}$ values are generally lower for fl-DHX8 compared with DHX8Δ547, but our results clearly show that a strand of four nucleotides is the minimum size required for productive RNA binding.

The structure of DHX8Δ547 reveals unexpected flexibility in the DEAH motif

To elucidate the molecular mechanisms underlying DHX8 function, we attempted to crystallise fl-DHX8, but this was unsuccessful probably due to the possibly unstructured nature of the N-terminal domain. However, we successfully crystallised DHX8Δ547 in the presence of ADP-Mg^{2+} and solved its structure bound to ADP using a 2.6 Å dataset. The DHX8Δ547-ADP structure consists of four similar independent DHX8Δ547 molecules and was refined to R_{work} and R_{free} values of 18.1 and 21.4%, respectively (Supplementary Table S1). Subsequently, we were able to determine the DHX8Δ547-ADP structure at 2.3 Å resolution, and refined it to respective R_{work} and R_{free} values of 18.7 and 22.3% (Supplementary Table S1).

The two DHX8Δ547-ADP structures reveal a domain organisation very similar to that of other DEAH-box helicases (Figure 5A) [25,35,50]. DHX8Δ547 adopts a pyramidal-like structure with the two N-terminal RecA domains and the C-terminal ratchet-like and OB-fold domains on opposite sides of the putative DHX8 RNA-binding tunnel, and the C- and N-terminal domains connected by the WH domain. A 26 Å long antiparallel β-hairpin, characteristic of the DEAH helicase family [25,26,35,50,55], extends from RecA2 and interacts with a C-terminal region between the WH and OB-fold domains.

Biochemical Journal (2019) **476** 2521–2543
https://doi.org/10.1042/BCJ20190383

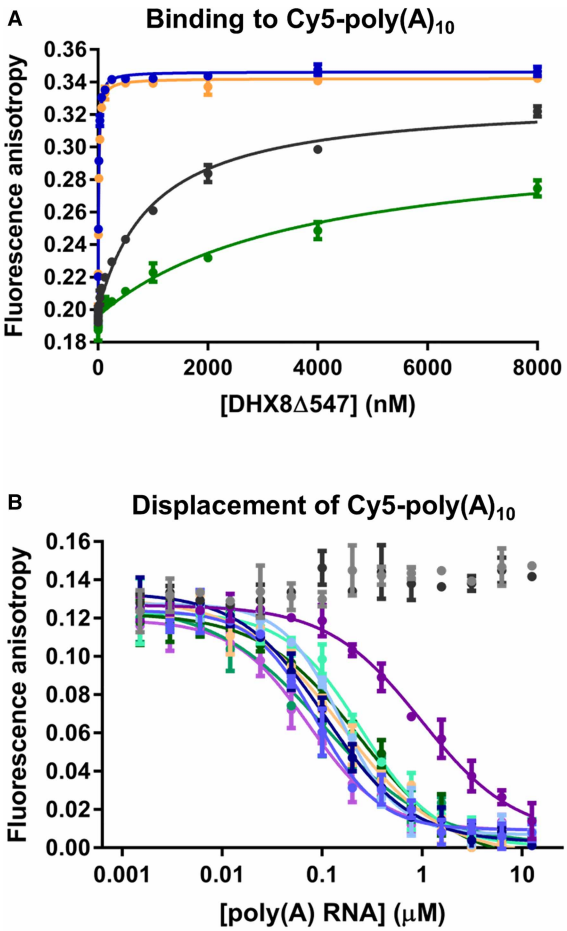

Nucleotide	K_d for Cy5-poly(A)$_{10}$ (nM) DHX8Δ547	fl-DHX8
No nucleotide	981 ±173	>4000
ADP	>4000	>4000
ADP-AlF$_x$	7.1 ±1.9	12 ±6
ADP-BeF$_3$	10 ±4	6.4 ±1.2

poly(A) RNA	DHX8Δ547 IC_{50} (nM)	fl-DHX8 IC_{50} (nM)
A_2	>10000	>10000
A_3	>10000	>10000
A_4	1083 ±367	1090 ±372
A_5	88 ±1	42 ±7
A_6	126 ±18	37 ±6
A_7	173 ±30	51 ±3
A_8	182 ±37	45 ±14
A_9	292 ±66	49 ±13
A_{10}	273 ±86	91 ±67
A_{15}	83 ±27	82 ±43
A_{20}	44 ±26	68 ±41

Figure 3. Characterisation of DHX8 binding to poly(A) RNA.

(**A**) FA data for DHX8Δ547 titrated against Cy5-poly(A)$_{10}$ in the absence of nucleotide or in the presence of 2 mM ADP, ADP-BeF$_3$ or ADP-AlF$_x$. Data are fitted to a quadratic binding equation and the K_d values shown in the table. K_d values >4000 nM are too weak to be accurately determined. (**B**) Displacement of Cy5-poly(A)$_{10}$ from DHX8Δ547 by different lengths of poly(A) RNA in the presence of 2 mM ADP-AlF$_x$. Cy5-poly(A)$_{10}$ background fluorescence has been subtracted for all data points. The calculated IC_{50} values are shown in the table. IC_{50} values >10 000 nM are too weak to be accurately determined. Graphical data are representative of three independent experiments. K_d and IC_{50} values are the averages from three independent experiments ± standard deviations. Graphs for fl-DHX8 are shown in Supplementary Figure S3C,E.

The ADP molecule bound in the ATP-binding site between the DHX8 RecA1 and RecA2 domains has a binding mode similar to the one observed for Prp43 and DHX15 [25,29,56]. However, two distinct conformations of the ADP adenine ring are observed (Figure 5B and Supplementary Figure S4A). In both conformations, the adenine ring stacks between R629 from RecA1 and F825 from RecA2 and forms a hydrogen bond between its 6-amino group and the main chain carbonyl of S625 in RecA1. However, in some of the DHX8 chains, the adenine N3 also interacts with the DHX8 main chain, most often with the amide group of T847 via a water-mediated hydrogen bond. The observed flexibility in the adenine conformation, combined with the limited number of direct protein–nucleotide hydrogen bonds, is consistent with our FA data showing that DHX8 can bind all NDP nucleotides. The 2′- and 3′-hydroxyl groups of the ribose form hydrogen bonds with the side chains of D849 and R893 in RecA2. The α- and β-phosphates are buried deep within the protein and form extensive interactions with the P-loop (motif I) in RecA1. The extensive coordination of the β-phosphate corroborates the observation that it is crucial for DHX8 nucleotide binding in our FA assays.

Biochemical Journal (2019) **476** 2521–2543
https://doi.org/10.1042/BCJ20190383

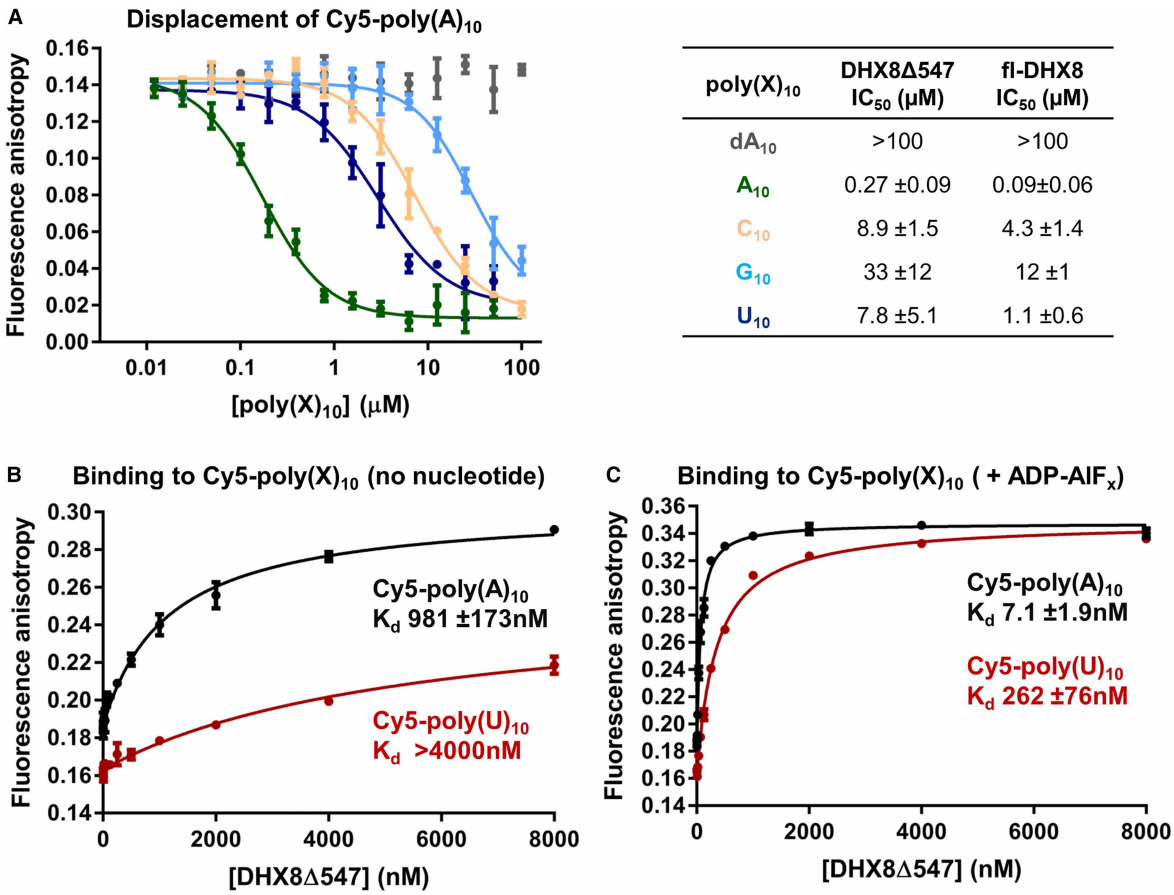

poly(X)$_{10}$	DHX8Δ547 IC$_{50}$ (μM)	fl-DHX8 IC$_{50}$ (μM)
dA$_{10}$	>100	>100
A$_{10}$	0.27 ±0.09	0.09±0.06
C$_{10}$	8.9 ±1.5	4.3 ±1.4
G$_{10}$	33 ±12	12 ±1
U$_{10}$	7.8 ±5.1	1.1 ±0.6

Figure 4. Comparison of DHX8 binding to poly(A) with poly(X) RNA.

(**A**) Displacement of Cy5-poly(A)$_{10}$ from DHX8Δ547 by unlabelled poly(X)$_{10}$ DNA or RNA in the presence of 2 mM ADP-AlF$_x$. Cy5-poly(A)$_{10}$ background fluorescence has been subtracted. The calculated IC$_{50}$ values are shown on the right-hand side. IC$_{50}$ values >100 μM are too weak to be accurately determined. Graphs for fl-DHX8 are shown in Supplementary Figure S3D. (**B**) FA data for DHX8Δ547 titrated against Cy5-poly(X)$_{10}$ in the absence of nucleotide or in the presence of 2 mM ADP-AlF$_x$. (**C**) Data are fitted to a quadratic binding equation, K_d values >4000 nM are too weak to be accurately determined. Graphical data are representative of three independent experiments. K_d and IC$_{50}$ values are the averages from three independent experiments ± standard deviations.

In the 2.6 Å structure, the DEAH motif (motif II) adopts the same conformation as observed in Prp43 and DHX15 ADP-bound structures [25,29], with D685 and E686 coordinating the magnesium–water constellation that stabilises the ADP-phosphate group, and H688 orienting the side chain of E686. However, in all four independent DHX8Δ547 molecules in the 2.3 Å DHX8Δ547-ADP structure, the conformation of the DEAH motif deviates significantly from that observed in the 2.6 Å DHX8Δ547-ADP structure (Figure 5C,D). While D685 is in its previously observed orientation, coordinating the Mg^{2+} ion by a water-mediated interaction, H688 adopts a different conformation and forms a hydrogen bond with the main chain carbonyl of D685 in three of the four DHX8 molecules (chains A, C, D). This interaction distorts the geometry of the DEAH motif and disrupts the hydrogen bond between H688 and E686. This results in a 5 Å movement of E686 to the location previously occupied by the side chain of H688, which is incompatible with stabilisation of the Mg^{2+} ion. In the fourth molecule (chain B), H688 is in its original conformation, but E686 adopts another different conformation and interacts with the backbone amide groups of H688 and E689, also incompatible with the stabilisation of the Mg^{2+} ion. The flexibility in the DEAH motif is corroborated by the B-factors of its residues E686, A687 and H688, which are ∼1.5 times higher than the average for the other residues of the same chain (Supplementary

Biochemical Journal (2019) **476** 2521–2543
https://doi.org/10.1042/BCJ20190383

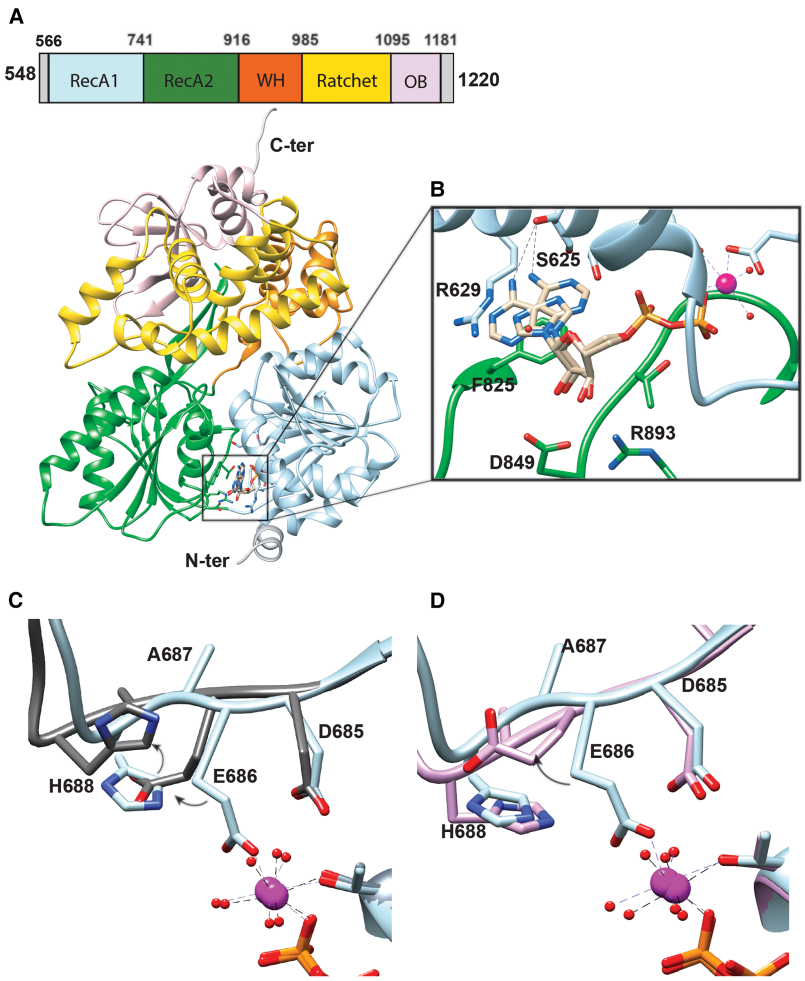

Figure 5. Crystal structures of DHX8Δ547 bound to ADP.

(**A**) Overall structure of DHX8Δ547-ADP. Domains are coloured according to the schematic shown above. (**B**) Close-up view of the ADP binding site in the 2.6 Å DHX8Δ547-ADP structure with the ADP adenine ring (in beige) adopting two conformations. (**C** and **D**) Alternative conformations of the DEAH motif (motif II) observed in the DHX8Δ547-ADP structures. Residues in blue represent the canonical DEAH conformation present in the 2.6 Å DHX8Δ547-ADP structure, grey the conformation observed in the 2.3 Å DHX8Δ547-ADP structure chains A, C and D, and pink the conformation observed in chain B. Side chain movements of E686 and H688 are highlighted by arrows. The coordination of the Mg^{2+} ion (magenta) is indicated by the dotted lines and water molecules are shown as red spheres.

Figure S5). To our knowledge, flexibility in motif II has not been observed for any other DEAH-box helicase, but could play a mechanistic role in the release of the ATP hydrolysis products.

Overall RNA binding mode is conserved between DHX8 and related SF2 helicases

To obtain a structural insight into DHX8 RNA binding, we soaked a DHX8Δ547 crystal, grown in the presence of ADP, with 1 mM poly$(A)_6$ single-strand RNA and determined the structure of DHX8Δ547 bound to poly $(A)_6$ RNA at 3.2 Å resolution (DHX8Δ547-A_6). This crystal belonged to space group $P2_12_12$ with two DHX8Δ547 molecules in the asymmetric unit and was refined to R_{work} and R_{free} values of 22.6 and 28.9%, respectively (Supplementary Table S1). The electron density for one of the copies (Chain C) was significantly weaker than for the other (Chain A); therefore, we modelled only its visible protein residues and parts of the RNA substrate. Consequently, all our structural analyses are based on chain A. As observed for other

Biochemical Journal (2019) 476 2521–2543
https://doi.org/10.1042/BCJ20190383

DEAH-box helicases, the poly(A)$_6$ RNA is bound in the central tunnel, flanked by the two RecA domains, WH, ratchet-like and OB-fold domains (Figure 6A and Supplementary Figure S4B). Compared with the DHX8Δ547-ADP structures, the C-terminal domains in DHX8Δ547-A$_6$ are rotated by ∼8° to open the channel and accommodate the RNA (Supplementary Figure S6A,B). The RNA is bound in an extended conformation with the 5′ end of its sugar–phosphate backbone binding to the RecA2 domain, and the 3′ end interacting with the RecA1 domain. The bases of nucleotides A3, A4, A5 and A6 are stacked against each other in the core of the RNA-binding channel and face the ratchet-like domain. A kink in the RNA between nucleotides A2 and A3 has flipped the bases of A1 and A2 at the 5′ end out of alignment with the A3–A6 base stack positioning them on the opposite side of the sugar–phosphate backbone. This RNA-binding mode, including the base stacking and position of the kink, is similar to that observed in other DExH helicase structures including ctPrp22-U$_9$, ctPrp43-ADP-BeF$_3$-U$_7$, scPrp43-ADPNP-U$_9$, MLE-ADPAlF$_4$-U$_{10}$ and viral NS3 helicases [27,28,35,50,57,58].

RNA binding triggers DEAH and P-loop movement and stimulates ADP release

Although DHX8Δ547-A$_6$ was obtained by soaking a DHX8Δ547-ADP crystal with poly(A)$_6$ RNA, no electron density for ADP-Mg^{2+} is present in the ADP binding site. This is most likely caused by an 8° rotation of the RecA domains with respect to each other, compared with their orientation in the DHX8Δ547-ADP structures, which has widened the adenine side of the ATP-binding site by ∼2.5–3 Å (Supplementary Figure S6A,B). As a result, motifs IV, IVa and V in the RecA2 domain have moved away from RecA1. However, the side chain of S845 in motif V in RecA2 still interacts with the side chain of D685 of the DEAH motif in RecA1 and this region adopts a more extended conformation than in DHX8Δ547-ADP and other DEAH-box helicase structures [35].

Unexpectedly, the P-loop in the DHX8 RecA1 domain has shifted into the phosphate-binding area adopting a conformation incompatible with nucleotide binding (Figure 6B,C). DHX8Δ547-A$_6$ also reveals conformational flexibility in the DEAH motif, different from that observed in the DHX8Δ547-ADP structures (Figure 6D). The electron density for the DEAH-motif residues is poor and the side chains cannot be modelled, indicating a mobility that together with the changes in P-loop conformation may have contributed to the release of ADP.

To investigate if the RNA-induced ADP release in the crystal also occurs in solution, we tested whether different lengths of poly(A) RNA could displace ATTO488-ATP from DHX8Δ547. Poly(A) RNA consisting of 4, 6, 8 or 10 nucleotides all caused displacement of the probe (Figure 6E). We therefore hypothesise that the RNA-stimulated conformational changes in the P-loop and DEAH motif of DHX8 are part of an active mechanism to release ADP, and that the DHX8Δ547-A$_6$ structure represents an intermediate state of DHX8 RNA translocation between the release of ADP and re-binding of ATP.

The RNA base stack is bookended by the β-hairpin and the hook-turn hairpin

The characteristic RNA base stack formed by nucleotides A3, A4, A5 and A6 is completely enclosed by the DHX8 RNA-binding tunnel (Figure 7A,B). The RecA domains interact with the RNA sugar–phosphate backbone of the stack primarily through residues from the helicase motifs Ia (R619, R620), Ib (T662, R668) and V (T839, N840). Additional interactions are made by the backbone amide groups of R647 and Q783, and the side chain of K861. Residues R619 and N840 form hydrogen bonds with the RNA 2′-hydroxyl groups of the ribose moieties of A4 and A3, respectively, explaining DHX8 selectivity for RNA over DNA (Figure 7A,D). Furthermore, the extensive stabilisation of these four nucleotides correlates with the minimum length of four nucleotides required for productive RNA binding in the FA assay.

The kink in the RNA at the 5′ end of the base stack and located at the base of the long β-hairpin in the DHX8 RecA2 domain is defined as a bookend in MLE and Prp43 [27,50]. The DHX8 β-hairpin interacts with RNA via a hydrophobic interaction between the adenine of A3 and L874, located in its second strand (Figure 7A,D). The A3 nucleotide is further anchored by K861 from the first strand of the β-hairpin, which forms a salt bridge with the A3 phosphate group, similar to the corresponding K853 in ctPrp22, K403 in ctPrp43, K398 in scPrp43 and R739 in MLE.

The bookend at the 3′ end of the base stack is formed by the hook-turn hairpin in RecA1 (also called the 3′-hairpin), but the interactions are different from those observed for Prp22, Prp43 and MLE [27,28,50]. In the ctPrp22, ctPrp43 and MLE structures, the arginine of the hook-turn interacts with a uracil base of the RNA and tilts the nucleotide towards the back of the RNA tunnel, while the adjacent phenylalanine stabilises the arginine conformation. The arginine side chain also interacts with a conserved glutamine residue from the ratchet-like domain (Q1073, Q627 and Q966, respectively; Supplementary Figure S6C). However, in DHX8, the adenine base of the corresponding nucleotide A6 is occupying the position of the hook-turn arginine side

Biochemical Journal (2019) **476** 2521–2543
https://doi.org/10.1042/BCJ20190383

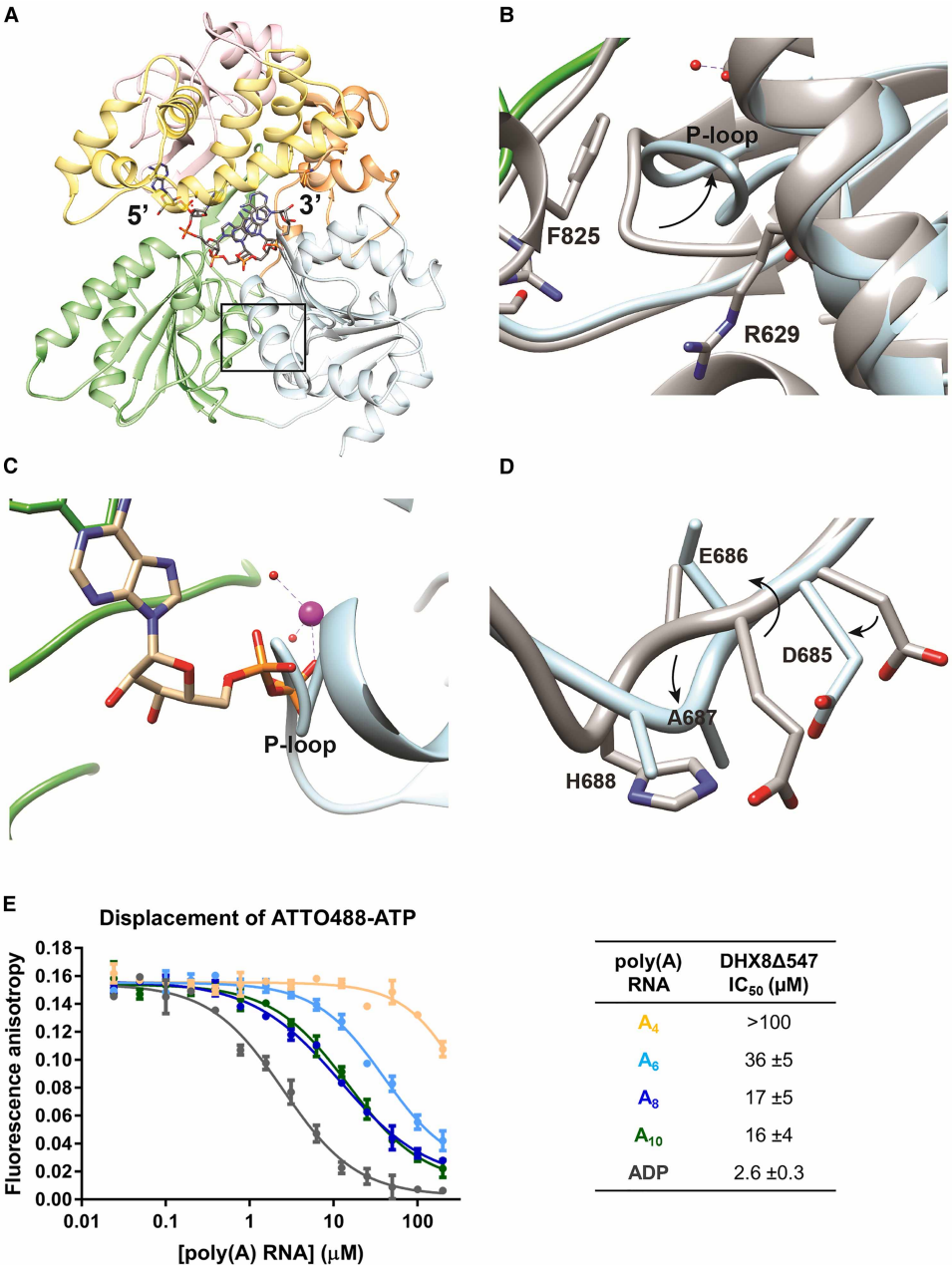

poly(A) RNA	DHX8Δ547 IC_{50} (μM)
A_4	>100
A_6	36 ±5
A_8	17 ±5
A_{10}	16 ±4
ADP	2.6 ±0.3

Figure 6. RNA binding to DHX8Δ547 causes ADP release.

(**A**) Overall structure of DHX8Δ547-A_6 with poly(A)$_6$ RNA shown in dark grey. (**B**) Close-up showing the conformation of the P-loop (motif I) in DHX8Δ547-A_6 (blue) compared with the 2.6 Å DHX8Δ547-ADP structure (grey). Superposition of DHX8Δ547-A_6 with ADP from the 2.6 Å DHX8Δ547-ADP structure in (**C**) shows that the P-loop adopts a conformation incompatible with nucleotide binding. (**D**) Mobility in the DEAH motif in DHX8Δ547-A_6. Residues in grey represent the canonical DEAH conformation in the 2.6 Å DHX8Δ547-ADP structure; light blue shows the DEAH motif conformation observed in DHX8Δ547-A_6. The black box in **A** highlights the region corresponding to the close-ups in (**B–D**). (**E**) FA assay showing the displacement of ATTO488-ATP from DHX8Δ547 by poly(A) RNA. ATTO488-ATP is hydrolysed before the experiment reaches equilibrium and therefore represents ATTO488-ADP. ATTO488-ATP background fluorescence has been subtracted. The calculated IC_{50} values are shown on the right-hand side. The IC_{50} curve and value for ADP is included for comparison. Data are representative of three independent experiments. IC_{50} values are averages from three independent experiments ± standard deviations.

Biochemical Journal (2019) **476** 2521–2543
https://doi.org/10.1042/BCJ20190383

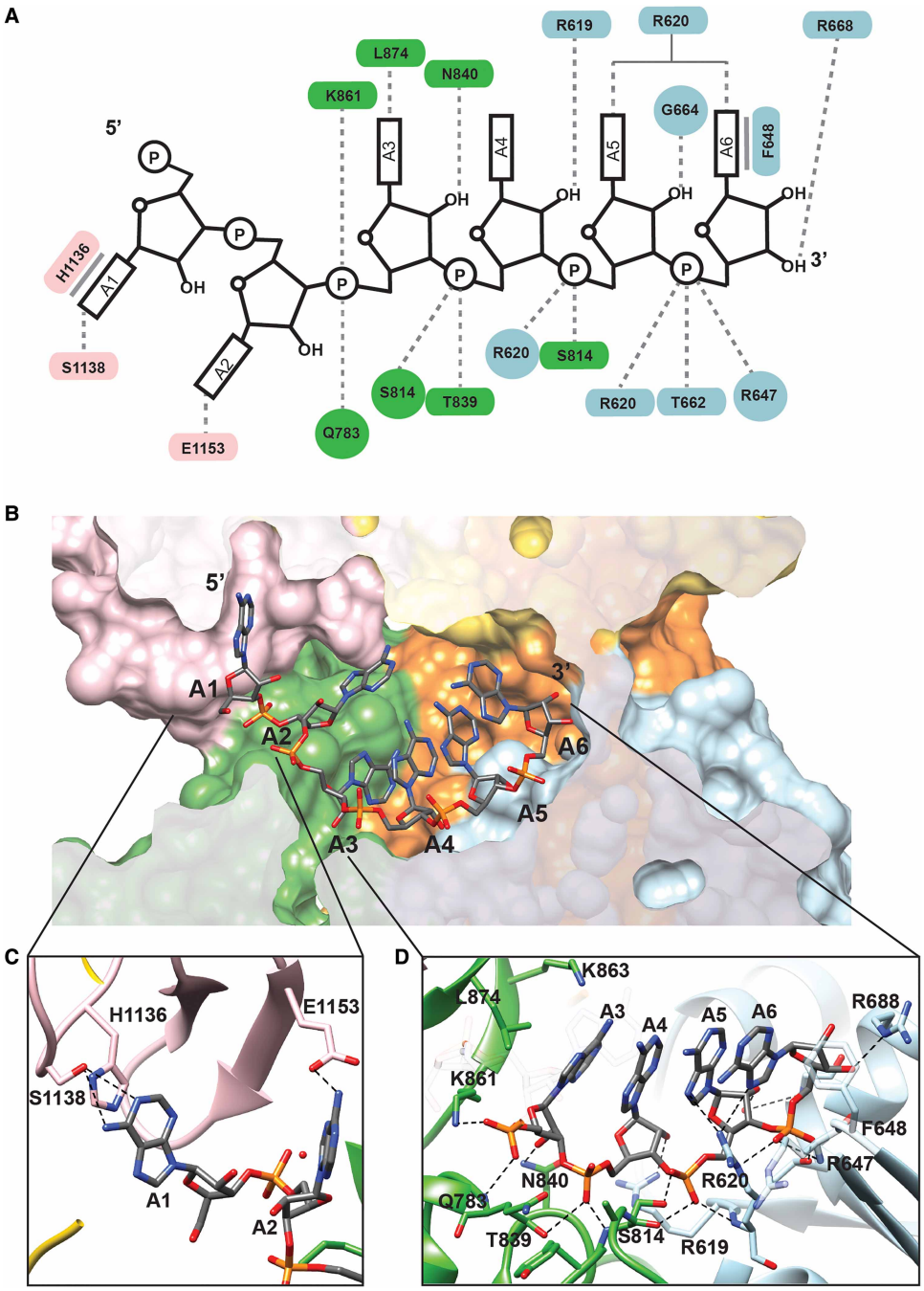

Figure 7. Molecular details of RNA binding to DHX8.

(**A**) DHX8Δ547-RNA interactions. Residues forming main chain interactions with RNA are shown as circles and residues forming side chain interactions as ellipses. Polar contacts are indicated by dotted lines and stacking interactions by thick lines. The interaction of G664 with the 2′OH group of A5 is mediated by a water molecule. (**B**) Surface representation of the DHX8 RNA-binding channel with poly(A)$_6$ RNA shown in grey. (**C**) Base-specific interactions in the DHX8 OB-fold domain. (**D**) The RNA base stack formed by nucleotides A3, A4, A5 and A6. The base stack is bookended by interactions with K861 and L874 from the RecA2 β-hairpin at the 5′ end and by interactions with F648 of the RecA1 hook-turn hairpin at the 3′ end. In (**C**) and (**D**), key residues are labelled and shown as sticks. Polar DHX8 RNA interactions are indicated as dotted lines.

chain in the other structures and is in better alignment with the rest of the base stack (Supplementary Figure S7A). The side chain of phenylalanine F648 interacts directly with the adenine of A6, via edge-face stacking (Figures 7A and 9A) and is stabilised by a hydrophobic interaction with I1078 from the ratchet-like domain. To accommodate the A6 adenine, the side chain of R647 has moved away from the RNA-binding channel. In this conformation, R647 does not interact with Q1081, the conserved glutamine in the DHX8 ratchet helix. These hook-turn side chain orientations are accompanied by a twist in its backbone when compared with the more regular β-hairpin conformation in the DHX8Δ547-ADP and the ctPrp22, ctPrp43 and MLE RNA-bound structures (Supplementary Figure S6C,D). The different interactions between the hook-turn and ratchet helix in these structures suggest a synchronised movement between the ratchet-like and RecA1 domains during RNA disruption, while the variations in hook-turn–RNA interactions suggest that this motif is dynamically involved in correctly orienting the bases for directional RNA movement through the RNA-binding tunnel.

DHX8 forms RNA base-specific interactions through its OB-fold and RecA1 domains

In addition to the stabilisation of the RNA sugar–phosphate backbone and the contacts with the 3′- and 5′-RNA bookends, DHX8 forms specific interactions with the respective N7 atoms of both adenine A5 and A6 in the RNA-stack, via the side chain of R620 of motif Ia (Figure 7A,D). Intriguingly, in the DHX8Δ547-ADP structures, the side chain of R620 forms a bidentate hydrogen bond with the backbone carbonyl groups of S814 and L816 of motif IVa in RecA2 (also known as the hook-loop, Supplementary Figure S7B). Thus, the significant movement of R620 and its key location between the RNA-binding tunnel and ATP-binding site suggest that it may act as an RNA sensor and facilitate allosteric communication between the sites. Indeed, mutation of R620 to alanine reduced both ATP and RNA binding affinity and impaired nucleic acid duplex separation activity (Figure 8A and C–E). In addition, DHX8Δ547-R620A showed lower RNA-stimulated ATPase activity than wild-type DHX8Δ547 (Figure 8B and Table 1), consistent with reduced RNA-binding affinity.

The DHX8 OB-fold also forms base-specific interactions with the A1 and A2 nucleotides that precede the RNA kink at the β-hairpin bookend. The orientation of A1 and A2 is completely different from the nucleotides in the stack, as highlighted by an angle of ∼115° between the adenine of A2 and A3 (Figure 7B,C). The adenine bases of A1 and A2 do not stack against each other but are oriented at an angle of ∼50°; however, both bases interact with residues in the DHX8 OB-fold domain. The adenine of A2 forms a bidentate hydrogen bond between its 6-amino group and the E1153 carboxylate, and the base of A1 interacts with the S1138 hydroxyl through both its 6-amino and N1 atoms. The A1 base is further stabilised by a π-stacking interaction with H1136 (Figure 7A,C). The base-specific interactions are consistent with the observed preference of DHX8 for adenine-rich ssRNA in our *in vitro* FA assay, and show how its OB-fold domain assists in guiding RNA through the RNA-binding tunnel.

DHX8 requires both its hook-turn and hook-loop for helicase activity

In addition to the hook-turn hairpin in RecA1, the RNA-bound structure of MLE also highlighted a β-hairpin in RecA2 (the hook-loop) as a key structural motif in the RNA translocation mechanism of DEAH-box helicases [50]. In MLE, the side chains of both the hook-loop and hook-turn interact directly with RNA. Mutation of the three hook-loop residues to glycine impaired duplex unwinding, verifying its functional role. In Prp43, the side chains of the hook-loop point away from the bound RNA and mutation of these residues had no significant effect on Prp43 RNA unwinding or RNA-stimulated ATP hydrolysis [28]. In contrast, mutation of the two hook-turn residues to glycine abolished both Prp43 unwinding activity and RNA-stimulated hydrolysis, which led to the suggestion that MLE and Prp43 differ in the details of their respective unwinding mechanisms [28].

Unlike the hook-turn, the sequence of the hook-loop varies across the DEAH-box family (Supplementary Figure S8A,B), but the backbone conformation of the DHX8Δ547-A_6 hook-loop is comparable to that observed in the Prp43 and MLE RNA-bound structures (Supplementary Figure S7C). Similar to MLE, the DHX8 hook-loop interacts directly with the RNA through a hydrogen bond between the side chain of S814 and the RNA sugar–phosphate backbone (Figures 7A,D and 9A).

To functionally examine the roles of the hook-loop and hook-turn in DHX8 helicase activity, we introduced the equivalent hook-loop (Y813G, S814G, A815G) and hook-turn (R647G, F648G) mutations in DHX8Δ547 (DHX8Δ547-HL and DHX8Δ547-HT, respectively) and characterised them in our *in vitro* assays. Both

Biochemical Journal (2019) **476** 2521–2543
https://doi.org/10.1042/BCJ20190383

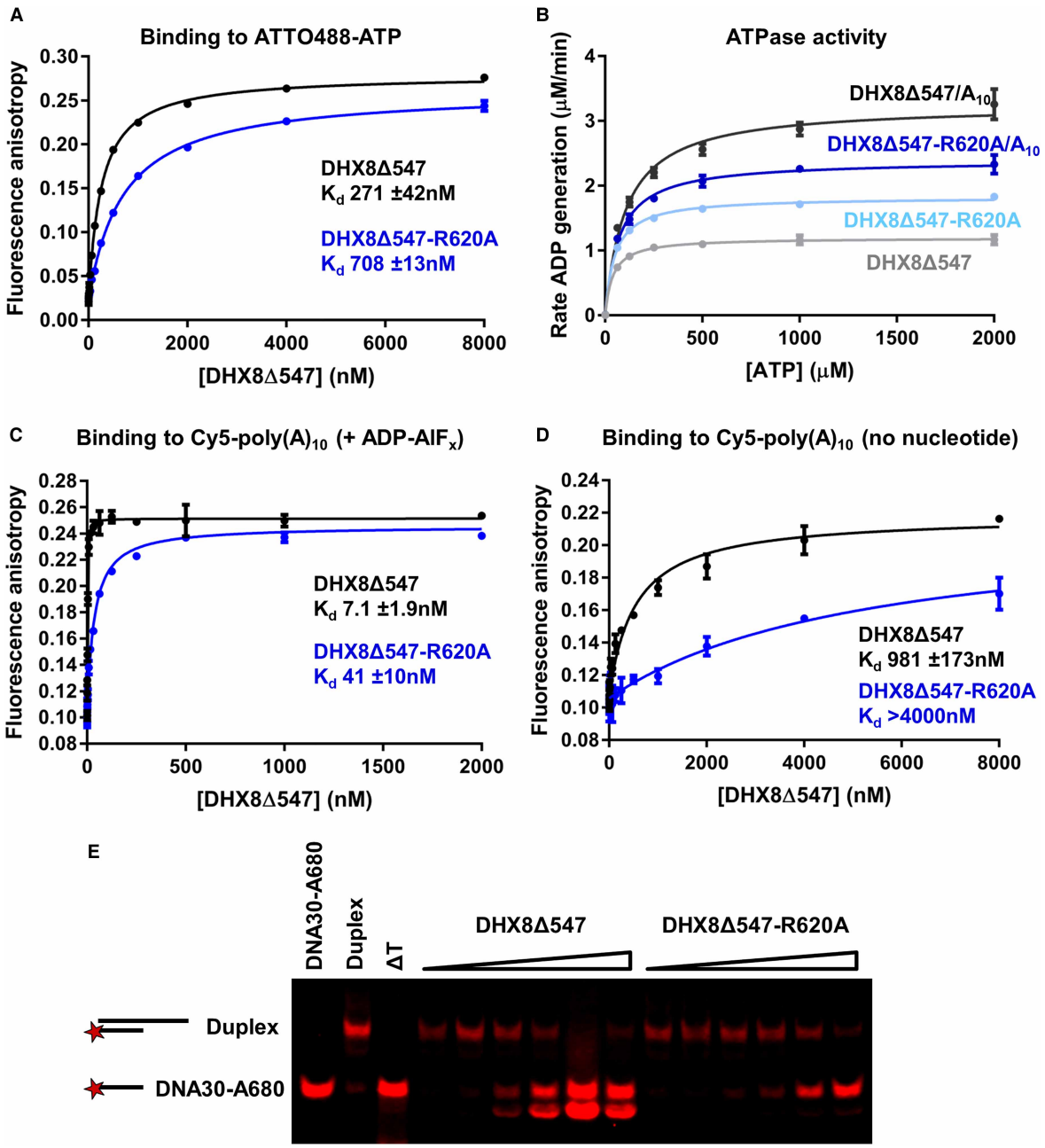

Figure 8. DHX8 residue R620 of motif Ia is involved in ATP binding, RNA binding and nucleic acid unwinding.
(**A**) ATTO488-ATP binding to DHX8Δ547-R620A compared with wild-type. Data are fitted to a quadratic binding equation. (**B**) ATPase activity of DHX8Δ547-R620A compared with wild-type in the absence and presence of poly(A)$_{10}$ RNA. Data are fitted using the Michaelis–Menten model and kinetic parameters shown in Table 1. (**C** and **D**) FA data for DHX8Δ547-R620A binding to Cy5-poly(A)$_{10}$ in the presence of 2 mM ADP-AlF$_x$ or in the absence of nucleotide, respectively. Data are fitted to a quadratic binding equation. (**E**) DHX8Δ547-R620A unwinding activity compared with that of wild-type. DHX8Δ547 concentrations of 10, 20, 50, 100, 200, and 500 nM unwind an RNA/DNA duplex (10 nM), but DHX8Δ547-R620A exhibits impaired duplex unwinding. Data are representative of three independent experiments. K_d values are the averages from three independent experiments ± standard deviations.

Biochemical Journal (2019) **476** 2521–2543
https://doi.org/10.1042/BCJ20190383

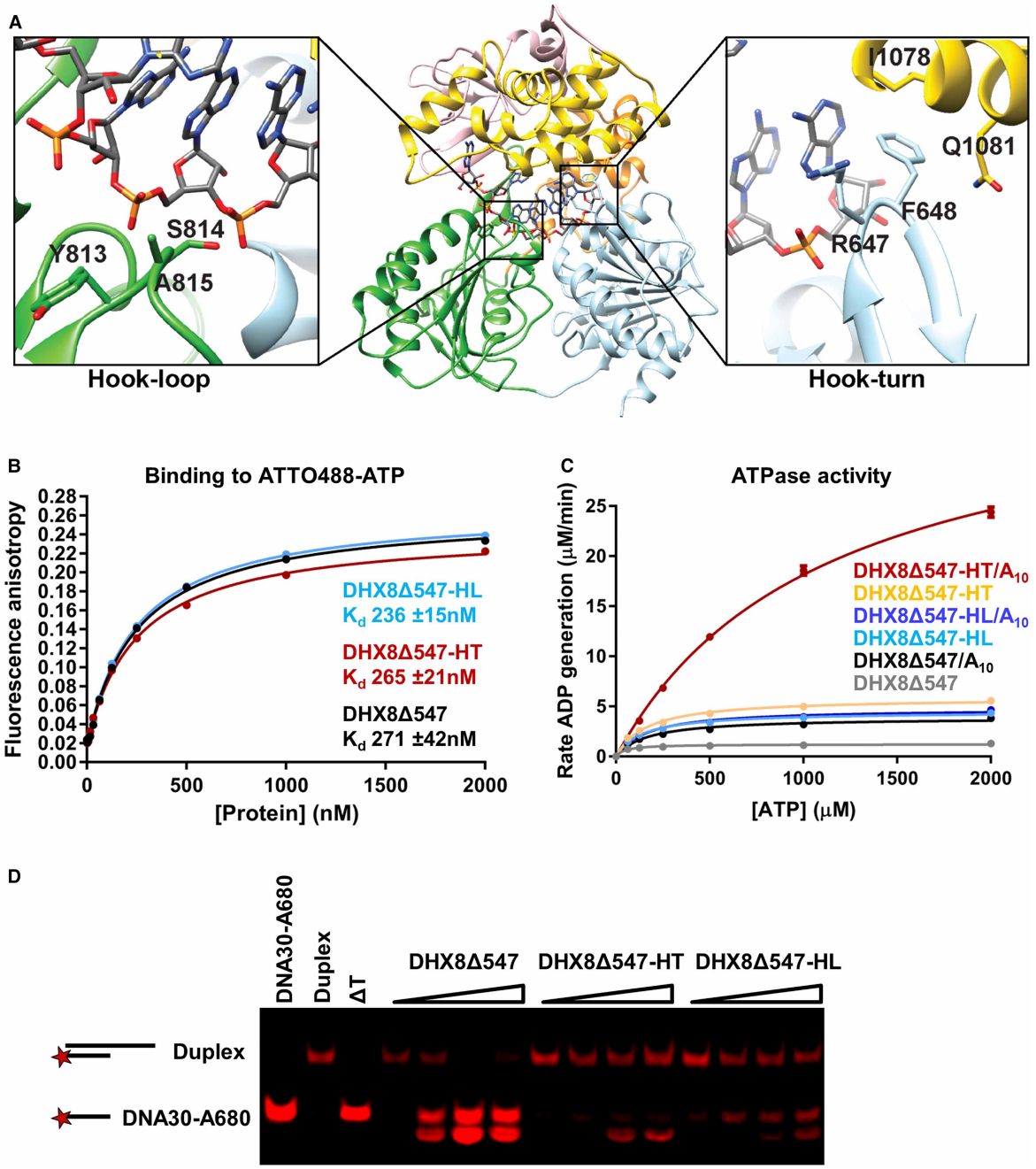

Figure 9. DHX8 requires both its hook-loop and hook-turn for enzymatic activity.

(**A**) The hook-loop (RecA2) and hook-turn (RecA1) regions and their location in DHX8Δ547-A_6. The side chain of R647 in the hook-turn has moved to accommodate the A6 adenine, which is face-edge stacked by F648. (**B**) ATTO488-ATP binding to the DHX8Δ547-HL and DHX8Δ547-HT mutants. Data are fitted to a quadratic binding equation. The curves for DHX8Δ547 and DHX8Δ547-HL are overlaid with each other. (**C**) ATPase activity of DHX8Δ547-HL and DHX8Δ547-HT in the absence and presence of poly$(A)_{10}$ RNA. Data are fitted using the Michaelis–Menten model and kinetic parameters shown in Table 1. (**D**) DHX8Δ547 unwinding activity compared with that of the DHX8Δ547-HT and DHX8Δ547-HL mutants. DHX8Δ547 concentrations of 10, 100, 200, 500 nM unwind an RNA/DNA duplex (10 nM), but DHX8Δ547-HT and DHX8Δ547-HL show significantly impaired duplex unwinding. Data are representative of at least two independent experiments. K_d values are the averages from two independent experiments ± standard deviations.

Biochemical Journal (2019) **476** 2521–2543
https://doi.org/10.1042/BCJ20190383

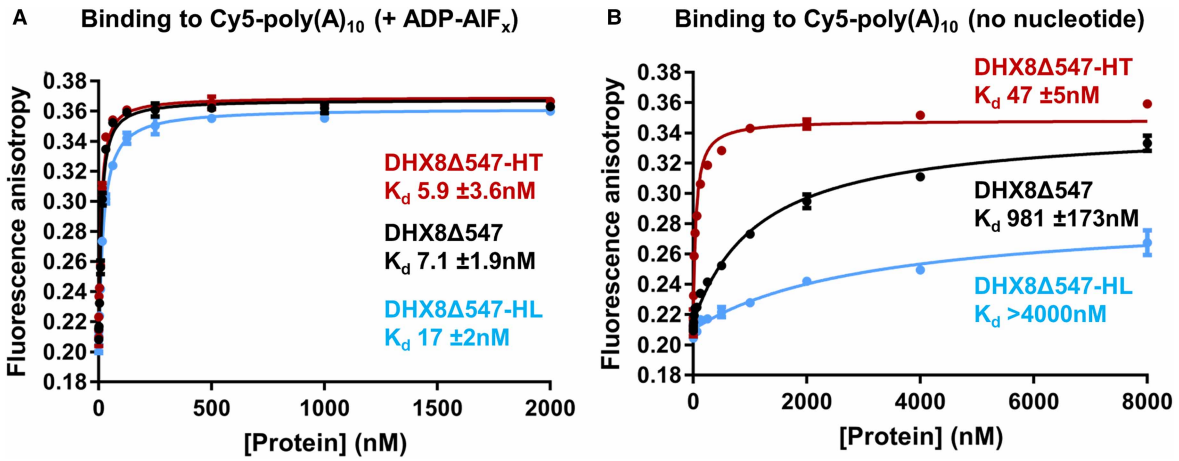

Figure 10. DHX8Δ547-HT and DHX8Δ547-HL binding to RNA.

FA data for DHX8Δ547-HT and DHX8Δ547-HL binding to Cy5-poly(A)$_{10}$ in the presence of 2 mM ADP-AlF$_x$ (**A**) or in the absence of nucleotide (**B**). Data are fitted to a quadratic binding equation. Data are representative of two independent experiments, K_d values are averages of two independent experiments ± standard deviations.

DHX8Δ547 mutants had the same melting temperature as wild-type protein (Supplementary Figure S9) and bound to the ATTO488-ATP probe with comparable affinity (Figure 9B), confirming that they are correctly folded.

Both DHX8Δ547-HL and DHX8Δ547-HT have impaired duplex unwinding activity compared with wild-type DHX8Δ547 (Figure 9D), suggesting that the hook-loop and hook-turn are both important for DHX8 helicase function. The reduction in duplex unwinding is not a result of diminished ATP hydrolysis as both mutants have increased basal ATPase activity compared with wild-type (3.4-fold and 5.4-fold over wild-type, respectively, Table 1, Figure 9C). However, while DHX8Δ547-HT ATPase activity was stimulated 6.7-fold by RNA, compared with 2.8-fold for wild-type, DHX8Δ547-HL was not stimulated in the presence of RNA. This indicates that the hook-loop and hook-turn mutations interfere with the coupling of ATP hydrolysis to productive nucleic acid unwinding.

Analysis in the RNA FA assay demonstrated that in the presence of ADP-AlF$_x$, both DHX8Δ547-HL and DHX8Δ547-HT are still able to bind RNA with nanomolar affinities (K_d's = 17 and 5.9 nM, respectively) similar to wild-type DHX8Δ547 (Figure 10A). In the absence of nucleotide, DHX8Δ547-HT has much higher affinity for Cy5-poly(A)$_{10}$ (K_d = 47 nM) than wild-type DHX8Δ547 (K_d = 981 nM), but DHX8Δ547-HL RNA binding is severely weakened (K_d > 4000 nM, Figure 10B). This suggests that DHX8Δ547-HT and DHX8Δ547-HL may impair duplex separation by disrupting the cycle of alternating strong and weak RNA binding events during ATP hydrolysis. Taken together the duplex unwinding, ATPase and RNA binding activities of DHX8Δ547-HL and DHX8Δ547-HT confirm that both the hook-loop and hook-turn play crucial roles during DHX8 helicase function.

Discussion

Insight into the underlying mechanisms of splicing has increased significantly in recent years, but the human DEAH-box helicases remain poorly characterised. Here, we have described the first high-resolution crystal structures and biochemical characterisation of catalytically active DHX8, a human DEAH helicase required for the release of mature mRNA from the spliceosome.

Our structures and biochemical data reveal insights into the mechanism of ADP release, the roles of R620, the hook-turn and the ratchet helix, and highlight the intricate communication between the DHX8 NTP and RNA binding sites. The variation of DHX8 affinity for RNA in the presence of the ATP mimics ADP-AlF$_x$ and ADP-BeF$_3$, compared with ADP or no nucleotide, is consistent with an ATP-driven RNA translocation mechanism via a series of alternating strong and weak RNA binding events. This is in agreement with the translocation mechanism proposed for ctPrp22, enabling DHX8 and Prp22 to act as molecular winches that pull apart RNA–RNA and RNA–protein interactions distal from their respective locations at the periphery of the spliceosome [14,59].

Our finding that a minimum of four nucleotides is required for productive RNA binding, but RNA binding affinity increases over 10-fold with five nucleotides, is consistent with proposed RNA translocation models for DEAH-box helicases involving a step size of one RNA nucleotide per molecule of ATP hydrolysed, and alternation between a four- and five-nucleotide central base stack [27,35].

The *in vitro* preference of DHX8 for poly(A) RNA substrates is in agreement with base-specific interactions identified in the RNA-bound DHX8Δ547-A_6 crystal structure. However, the spliceosomal helicases are thought to be sequence non-specific because of the wide variety of RNA substrates they need to process. Indeed, the residues H1136, S1138 and E1153 from the DHX8 OB-fold domain that make base-specific contacts with RNA are conserved across DEAH-box helicases; however, in ctPrp22 and Prp43, the equivalents of S1138 and E1153 do not contact the bound RNA, or only interact with the RNA backbone. In addition, H1136 forms a similar stacking triad with P1137 and F1142 to the one observed in ctPrp22 which interacts with polyU RNA. Therefore, while these interactions confirm that the DHX8 OB-fold is important in guiding RNA through the RNA tunnel, it remains to be determined whether DHX8 *in vitro* specificity for adenine-rich RNA points to a specific cellular function, or reflects its adaptability to different RNA substrates.

During preparation of this paper, the structure of Prp22 from the fungus *C. thermophilum* bound to poly $(U)_9$ RNA was published. In that structure, the RecA domains adopt an open conformation accommodating a central RNA base stack comprising five nucleotides. Compared with our DHX8Δ547-ADP structures, the RecA domains in DHX8Δ547-A_6 are also in an open conformation, but the opening is not as wide as in the ctPrp22 structure (Supplementary Figure S10A,B). Consequently, the RNA base stack contains only four nucleotides, as is also observed in the ADP-BeF_3- and ADP-AlF_x-bound Prp43 and MLE structures. Our DHX8Δ547-A_6 structure therefore represents an earlier snapshot in the RNA translocation cycle, just after ATP hydrolysis and ADP release, but before the RecA domains have fully opened to enable incorporation of the fifth nucleotide into the RNA base stack. However, the region around S845 in motif V adopts an extended conformation in DHX8Δ547-A_6 and the small α-helix proposed to initiate the separation of the two RecA domains by steric hindrance [35] is not present (Supplementary Figure S10C).

A comparison of DHX8Δ547-A_6 with Prp22 in the context of the yeast spliceosome post-catalytic P complex [32] supports the proposal that our DHX8Δ547-A_6 structure is on a trajectory to a more fully opened state (Supplementary Figure S11), as the opening between the RecA domains of Prp22 in the yeast spliceosome is also more pronounced than that in DHX8Δ547-A_6. The combined structural data certainly demonstrate the extensive mechanical motions within these helicases that are crucial for their function as molecular winches.

The absence of ADP in the DHX8Δ547-A_6 structure, accompanied by the conformational flexibility in the DEAH motif and P-loop, suggests that these conformational changes are part of a mechanism for ADP release in DHX8, and this hypothesis is supported by our data demonstrating RNA-stimulated nucleotide release in solution. Interestingly, alternative conformations of the P-loop have been observed for NS3 helicases from Zika and Dengue virus [58,60] and therefore may be a general feature of the DExH-box helicases. However, to our knowledge, the flexibility in the DEAH motif has not previously been reported and further investigation is required to confirm if this is a more widespread occurrence within the DEAH-box family.

The molecular details of RNA-stimulated ADP release are not well understood, but it is clear that there is significant communication between the RNA- and NTP binding sites. A structural comparison between DHX8Δ547-ADP and DHX8Δ547-A_6 identified the conserved R620 of motif Ia as a likely candidate to relay the communication between the RNA and nucleotide binding sites due to its pivotal position at the interface between the RecA domains and the RNA-binding channel. In DHX8Δ547-A_6, the side chain of R620 interacts with two adenine bases of the RNA base stack. However, in ctPrp22, Prp43 and MLE, the corresponding arginine interacts with phosphates of the RNA backbone, or forms a hydrogen bond with the main chain of the adjacent hook-turn hairpin. In contrast, in the DHX8Δ547-ADP structures, the R620 side chain forms hydrogen bonds with carbonyl groups of S814 and L816 from the hook-loop in RecA2. Similar interactions are present in the Prp43 ADP-bound structures [25,29]. Mutation of R620 to alanine in DHX8 reduced both nucleotide and RNA binding and resulted in impaired duplex unwinding, thus confirming a previously unknown role in communication between the RNA and ATP-binding sites.

A crucial motif for RNA unwinding in DEAH-box helicases is the hook-turn hairpin [28,50]. The differences in conformations of the DHX8 hook-turn residues R647 and F648 and their interactions with RNA when compared with their equivalents in ctPrp22, Prp43 and MLE likely reflect the different states in RNA translocation that the respective structures represent. In addition, the unexpected plasticity in the conformation of R647 suggests a more dynamic role of the hook-turn in controlling directional movement of RNA through the

Biochemical Journal (2019) 476 2521–2543
https://doi.org/10.1042/BCJ20190383

RNA-binding tunnel than previously envisaged. The hook-turn in RecA1 appears to act as a gatekeeper positioning the nucleotide at the 3′ end of the RNA base stack for further movement through the RNA tunnel and, together with the β-hairpin in RecA2 at the 5′ end of the base stack and the stacking triad in the OB-fold domain, may prevent backsliding of the RNA. The twist in the hook-turn main chain in DHX8Δ547-A_6 causes a ripple effect of subtle changes throughout the RecA1 domain, that occur in concert with the conformational changes in the DEAH motif and P-loop, implying an additional role in communication between the RNA and ATP-binding sites. The differences in the interactions between the arginine of the hook-turn and glutamine in the ratchet helix in the RNA-bound DHX8Δ547-A_6, ctPrp22, ctPrp43 and MLE structures are intriguing as both residues are strictly conserved across the DEAH family (Supplementary Figure S8A,C). In addition, the corresponding residues to Q1081 in the Ski2-like helicases Hel308, Mtr4 and Brr2 have been identified as crucial for RNA unwinding [61–63]. This suggests that a concerted movement between the hook-turn and ratchet helix may be critical to relay intra-molecular motions between the RecA and ratchet-like domains during RNA translocation.

In DHX8, the hook-loop also interacts with the ratchet helix via a hydrogen bond between the carbonyl of A815 and R1070 at the ratchet's N-terminal end, and a similar interaction occurs between the carbonyl of L808 and R1062 in ctPrp22. The equivalent regions of the ratchet helices in Prp43, MLE and the Ski2-like helicases also interact with motifs in their RecA2 domains. This implies that while the details of the ratchet mechanisms differ between the Ski2-like and DEAH-box helicases, the ratchet helix is important in connecting the movements between the two RecA domains and communicating them to the auxiliary C-terminal regions in the wider helicase family. It is notable that of the five core domains in DEAH-box helicases, the WH domain moves the least between the different structural snapshots (Supplementary Figure S10A). This suggests that it acts as a hinge about which the RecA and C-terminal domains move in concert to thread RNA through the RNA-binding channel.

Our mutational studies demonstrate the involvement of both the hook-loop and hook-turn in DHX8 helicase activity. Both DHX8Δ547-HL and DHX8Δ547-HT have increased ATPase activity compared with wild-type DHX8Δ547, but are unable to translate ATP hydrolysis into nucleic acid duplex unwinding. The uncoupling of the two activities correlates with the roles of the hook-loop and hook-turn in communication between the RecA and ratchet domains. However, functional studies on MLE and Prp43 illustrate that small variations in amino acid sequence have significant effects on the detailed mechanism of helicase activity. Indeed, the sequence variation in the hook-loop is greater across the DEAH family than that of the hook-turn, suggesting that this region may be important in fine-tuning the helicase mechanism to the variety of biological roles of the different DEAH-box family members.

In conclusion, we have biochemically characterised human DHX8 and determined the first high-resolution crystal structure of its complete helicase domain in ADP and RNA-bound forms. Our data shed light on the mechanism of RNA-stimulated ADP release and highlight the roles of R620, the hook-loop, hook-turn and ratchet helix in enzymatic activity. Our results are consistent with the emerging function of DHX8 as a molecular winch able to disrupt RNA interactions distal to its peripheral location within the spliceosome. Finally, our findings on the structure and function of DHX8 may have therapeutic significance — especially in view of the importance of alternative splicing in human diseases, and the appreciation that helicases represent an underexploited class of druggable cancer targets [36,37].

Database Depositions

Atomic co-ordinates and structure factors for the reported crystal structures have been deposited with the Protein Data Bank under accession numbers 6HYS, 6HYT and 6HYU.

Abbreviations

EM, electron microscopy; ESRF, European Synchrotron Radiation Facility; FA, fluorescence anisotropy; FP, fluorescence polarisation; NMR, nuclear magnetic resonance; NTP, nucleotide triphosphate; OB, oligonucleotide binding; RMSD, root-mean-square deviation; RS, arginine-serine-rich; SF2, superfamily 2; snRNP, small nuclear ribonucleoprotein; WH, winged-helix.

Author Contributions

C.F.-R., J.C.T. and C.McA. carried out cloning, protein expression and purification. J.C.T. performed the biochemical assays and J.C.T. and R.B. conducted the interpretation of the assay data. C.F.-R. carried out all

crystallisation and structure determination and Y.-V.L.B. assisted in refinement of the structures. Crystal structure analysis was done by C.F.-R., J.C.T. and R.L.M.v.M.; C.F.-R., J.C.T., P.W. and R.L.M.v.M. wrote the paper and supervised the research.

Funding

This work was supported by Cancer Research U.K. [grant numbers C309/A11566, C2739/A22897]. We are grateful for the support of the ICR's Faringdon Fund. P.W. is a Cancer Research UK Life Fellow.

Acknowledgements

We thank Dr Paul Clarke for helpful discussions about spliceosomal helicases, and Dr Nora Cronin and the staff of the ESRF for their support during data collection.

Competing Interests

The authors are employees of The Institute of Cancer Research, which has a commercial interest in the development of RNA helicase inhibitors. The authors have had research and licensing interactions with Astex Pharmaceuticals, AstraZeneca, Vernalis, Novartis, Cyclacel, Piramed Pharma, Genentech, Chroma Therapeutics, Merck Healthcare, Sareum, Sierra Oncology, Boston Pharmaceuticals, BTG, Cougar, J&J, and Carrick Pharmaceuticals. P.W. is a consultant/SAB member for Astex Pharmaceuticals, CV6 Therapeutics and NextechInvest; a stockholder in NextechInvest, STORM Therapeutics and Chroma Therapeutics; and also a Non-Executive Director of STORM Therapeutics and the Royal Marsden NHS Foundation Trust, and Board Member of the non-profit Chemical Probe Portal.

References

1 Kelemen, O., Convertini, P., Zhang, Z.Y., Wen, Y., Shen, M.L., Falaleeva, M. et al. (2013) Function of alternative splicing. *Gene* **514**, 1–30 https://doi.org/10.1016/j.gene.2012.07.083
2 Pan, Q., Shai, O., Lee, L.J., Frey, B.J. and Blencowe, B.J. (2008) Deep surveying of alternative splicing complexity in the human transcriptome by high-throughput sequencing. *Nat. Genet.* **40**, 1413–1415 https://doi.org/10.1038/ng.259
3 Tazi, J., Bakkour, N. and Stamm, S. (2009) Alternative splicing and disease. *Biochim. Biophys. Acta* **1792**, 14–26 https://doi.org/10.1016/j.bbadis.2008.09.017
4 Oltean, S. and Bates, D.O. (2014) Hallmarks of alternative splicing in cancer. *Oncogene* **33**, 5311–5318 https://doi.org/10.1038/onc.2013.533
5 Wang, B.D. and Lee, N.H. (2018) Aberrant RNA splicing in cancer and drug resistance. *Cancers* **10**, 458. https://doi.org/10.3390/cancers10110458
6 Wahl, M.C., Will, C.L. and Luhrmann, R. (2009) The spliceosome: design principles of a dynamic RNP machine. *Cell* **136**, 701–718 https://doi.org/10.1016/j.cell.2009.02.009
7 Papasaikas, P. and Valcarcel, J. (2016) The spliceosome: the ultimate RNA chaperone and sculptor. *Trends Biochem. Sci.* **41**, 33–45 https://doi.org/10.1016/j.tibs.2015.11.003
8 Cordin, O. and Beggs, J.D. (2013) RNA helicases in splicing. *RNA Biol.* **10**, 83–95 https://doi.org/10.4161/rna.22547
9 Liu, Y.C. and Cheng, S.C. (2015) Functional roles of DExD/H-box RNA helicases in pre-mRNA splicing. *J. Biomed. Sci.* **22**, 54 https://doi.org/10.1186/s12929-015-0161-z
10 Ono, W., Ohno, M. and Shimura, Y. (1994) Identification of a putative RNA helicase (Hrh1), a human homolog of yeast Prp22. *Mol. Cell Biol.* **14**, 7611–7620 https://doi.org/10.1128/MCB.14.11.7611
11 Ohno, M. and Shimura, Y. (1996) A human RNA helicase-like protein, HRH1, facilitates nuclear export of spliced mRNA by releasing the RNA from the spliceosome. *Gene Dev.* **10**, 997–1007 https://doi.org/10.1101/Gad.10.8.997
12 Mayas, R.M., Maita, H. and Staley, J.P. (2006) Exon ligation is proofread by the DExD/H-box ATPase Prp22p. *Nat. Struct. Mol. Biol.* **13**, 482–490 https://doi.org/10.1038/nsmb1093
13 Semlow, D.R. and Staley, J.P. (2012) Staying on message: ensuring fidelity in pre-mRNA splicing. *Trends Biochem. Sci.* **37**, 263–273 https://doi.org/10.1016/j.tibs.2012.04.001
14 Semlow, D.R., Blanco, M.R., Walter, N.G. and Staley, J.P. (2016) Spliceosomal DEAH-box ATPases remodel pre-mRNA to activate alternative splice sites. *Cell* **164**, 985–998 https://doi.org/10.1016/j.cell.2016.01.025
15 Park, J.W., Parisky, K., Celotto, A.M., Reenan, R.A. and Graveley, B.R. (2004) Identification of alternative splicing regulators by RNA interference in Drosphila. *Proc. Natl Acad. Sci. U.S.A.* **101**, 15974–15979 https://doi.org/10.1073/pnas.0407004101
16 English, M.A., Lei, L., Blake, T., Wincovitch, S.M., Sood, R., Azuma, M. et al. (2012) Incomplete splicing, cell division defects, and hematopoietic blockage in DHX8 mutant zebrafish. *Dev. Dynam.* **241**, 879–889 https://doi.org/10.1002/dvdy.23774
17 Fairman-Williams, M.E., Guenther, U.P. and Jankowsky, E. (2010) SF1 and SF2 helicases: family matters. *Curr. Opin. Struct. Biol.* **20**, 313–324 https://doi.org/10.1016/j.sbi.2010.03.011
18 Gilman, B., Tijerina, P. and Russell, R. (2017) Distinct RNA-unwinding mechanisms of DEAD-box and DEAH-box RNA helicase proteins in remodeling structured RNAs and RNPs. *Biochem. Soc. Trans.* **45**, 1313–1321 https://doi.org/10.1042/Bst20170095
19 Martin, A., Schneider, S. and Schwer, B. (2002) Prp43 is an essential RNA-dependent ATPase required for release of lariat-intron from the spliceosome. *J. Biol. Chem.* **277**, 17743–17750 https://doi.org/10.1074/jbc.M200762200
20 Tanaka, N. and Schwer, B. (2005) Characterization of the NTPase, RNA-binding, and RNA helicase activities of the DEAH-box splicing factor Prp22. *Biochemistry* **44**, 9795–9803 https://doi.org/10.1021/bi050407m

Biochemical Journal (2019) **476** 2521–2543
https://doi.org/10.1042/BCJ20190383

21 Lebaron, S., Papin, C., Capeyrou, R., Chen, Y.L., Froment, C., Monsarrat, B. et al. (2009) The ATPase and helicase activities of Prp43p are stimulated by the G-patch protein Pfa1p during yeast ribosome biogenesis. *EMBO J.* **28**, 3808–3819 https://doi.org/10.1038/emboj.2009.335

22 Robert-Paganin, J., Halladjian, M., Blaud, M., Lebaron, S., Delbos, L., Chardon, F. et al. (2017) Functional link between DEAH/RHA helicase Prp43 activation and ATP base binding. *Nucleic Acids Res.* **45**, 1539–1552 https://doi.org/10.1093/narlgkw1233

23 Wagner, J.D.O., Jankowsky, E., Company, M., Pyle, A.M. and Abelson, J.N. (1998) The DEAH-box protein PRP22 is an ATPase that mediates ATP-dependent mRNA release from the spliceosome and unwinds RNA duplexes. *EMBO J.* **17**, 2926–2937 https://doi.org/10.1093/emboj/17.10.2926

24 Schneider, S., Campodonico, E. and Schwer, B. (2004) Motifs IV and V in the DEAH box splicing factor Prp22 are important for RNA unwinding, and helicase-defective Prp22 mutants are suppressed by Prp8. *J. Biol. Chem.* **279**, 8617–8626 https://doi.org/10.1074/jbc.M312715200

25 Walbott, H., Mouffok, S., Capeyrou, R., Lebaron, S., Humbert, O., van Tilbeurgh, H. et al. (2010) Prp43p contains a processive helicase structural architecture with a specific regulatory domain. *EMBO J.* **29**, 2194–2204 https://doi.org/10.1038/emboj.2010.102

26 He, Y.Z., Andersen, G.R. and Nielsen, K.H. (2010) Structural basis for the function of DEAH helicases. *EMBO Rep.* **11**, 180–186 https://doi.org/10.1038/embor.2010.11

27 He, Y.Z., Staley, J.P., Andersen, G.R. and Nielsen, K.H. (2017) Structure of the DEAH/RHA ATPase Prp43p bound to RNA implicates a pair of hairpins and motif Va in translocation along RNA. *RNA* **23**, 1110–1124 https://doi.org/10.1261/rna.060954

28 Tauchert, M.J., Fourmann, J.B., Luhrmann, R. and Ficner, R. (2017) Structural insights into the mechanism of the DEAH-box RNA helicase Prp43. *eLife* **6**, e21510 https://doi.org/10.7554/eLife.21510

29 Murakami, K., Nakano, K., Shimizu, T. and Ohto, U. (2017) The crystal structure of human DEAH-box RNA helicase 15 reveals a domain organization of the mammalian DEAH/RHA family. *Acta Crystallogr. F Struct. Biol. Commun.* **73**, 347–355 https://doi.org/10.1107/S2053230X17007336

30 Fica, S.M., Oubridge, C., Galej, W.P., Wilkinson, M.E., Bai, X.C., Newman, A.J. et al. (2017) Structure of a spliceosome remodelled for exon ligation. *Nature* **542**, 377–380 https://doi.org/10.1038/nature21078

31 Bertram, K., Agafonov, D.E., Liu, W.T., Dybkov, O., Will, C.L., Hartmuth, K. et al. (2017) Cryo-EM structure of a human spliceosome activated for step 2 of splicing. *Nature* **542**, 318–323 https://doi.org/10.1038/nature21079

32 Liu, S., Li, X., Zhang, L., Jiang, J., Hill, R.C., Cui, Y. et al. (2017) Structure of the yeast spliceosomal postcatalytic P complex. *Science* **358**, 1278–1283 https://doi.org/10.1126/science.aar3462

33 Zhang, X., Yan, C., Hang, J., Finci, L.I., Lei, J. and Shi, Y. (2017) An atomic structure of the human spliceosome **169**, 918–929 e14 https://doi.org/10.1016/j.cell.2017.04.033

34 Kudlinzki, D., Schmitt, A., Christian, H. and Ficner, R. (2012) Structural analysis of the C-terminal domain of the spliceosomal helicase Prp22. *Biol. Chem.* **393**, 1131–1140 https://doi.org/10.1515/hsz-2012-0158

35 Hamann, F., Enders, M. and Ficner, R. (2019) Structural basis for RNA translocation by DEAH-box ATPases. *Nucleic Acids Res.* **47**, 4349–4362 https://doi.org/10.1093/nar/gkz150

36 Behan, F.M., Iorio, F., Picco, G., Goncalves, E., Beaver, C.M., Migliardi, G. et al. (2019) Prioritization of cancer therapeutic targets using CRISPR-Cas9 screens. *Nature* **568**, 511–516 https://doi.org/10.1038/s41586-019-1103-9

37 Patel, M.N., Halling-Brown, M.D., Tym, J.E., Workman, P. and Al-Lazikani, B. (2013) Objective assessment of cancer genes for drug discovery. *Nat. Rev. Drug. Discov.* **12**, 35–50 https://doi.org/10.1038/nrd3913

38 James, N.G. and Jameson, D.M. (2014) Steady-state fluorescence polarization/anisotropy for the study of protein interactions. *Methods Mol. Biol.* **1076**, 29–42 https://doi.org/10.1007/978-1-62703-649-8_2

39 Roehrl, M.H., Wang, J.Y. and Wagner, G. (2004) A general framework for development and data analysis of competitive high-throughput screens for small-molecule inhibitors of protein–protein interactions by fluorescence polarization. *Biochemistry* **43**, 16056–16066 https://doi.org/10.1021/bi048233g

40 Winter, G., Waterman, D.G., Parkhurst, J.M., Brewster, A.S., Gildea, R.J., Gerstel, M. et al. (2018) DIALS: implementation and evaluation of a new integration package. *Acta Crystallogr. D Struct. Biol.* **74**, 85–97 https://doi.org/10.1107/S2059798317017235

41 Evans, P.R. and Murshudov, G.N. (2013) How good are my data and what is the resolution? *Acta Crystallogr. D Biol. Crystallogr.* **69**, 1204–1214 https://doi.org/10.1107/S0907444913000061

42 Karplus, P.A. and Diederichs, K. (2012) Linking crystallographic model and data quality. *Science* **336**, 1030–1033 https://doi.org/10.1126/science.1218231

43 McCoy, A.J., Grosse-Kunstleve, R.W., Adams, P.D., Winn, M.D., Storoni, L.C. and Read, R.J. (2007) Phaser crystallographic software. *J. Appl. Crystallogr.* **40**, 658–674 https://doi.org/10.1107/S0021889807021206

44 Bricogne, G., Brandl M, B.E., Flensburg, C., Keller, P., Paciorek, W., Roversi, P. et al. (2017) *BUSTER 2.10.3*, Global Phasing Ltd, Cambridge, U.K.

45 Emsley, P., Lohkamp, B., Scott, W.G. and Cowtan, K. (2010) Features and development of Coot. *Acta Crystallogr. D Biol. Crystallogr.* **66**, 486–501 https://doi.org/10.1107/S0907444910007493

46 Davis, I.W., Leaver-Fay, A., Chen, V.B., Block, J.N., Kapral, G.J., Wang, X. et al. (2007) Molprobity: all-atom contacts and structure validation for proteins and nucleic acids. *Nucleic Acids Res.* **35**, W375–W383 https://doi.org/10.1093/nar/gkm216

47 Pettersen, E.F., Goddard, T.D., Huang, C.C., Couch, G.S., Greenblatt, D.M., Meng, E.C. et al. (2004) UCSF chimera — a visualization system for exploratory research and analysis. *J. Comput. Chem.* **25**, 1605–1612 https://doi.org/10.1002/jcc.20084

48 Jankowsky, E. (2011) RNA helicases at work: binding and rearranging. *Trends Biochem. Sci.* **36**, 19–29 https://doi.org/10.1016/j.tibs.2010.07.008

49 Schwer, B. and Gross, C.H. (1998) Prp22, a DExH-box RNA helicase, plays two distinct roles in yeast pre-mRNA splicing. *EMBO J.* **17**, 2086–2094 https://doi.org/10.1093/emboj/17.7.2086

50 Prabu, J.R., Muller, M., Thomae, A.W., Schussler, S., Bonneau, F., Becker, P.B. et al. (2015) Structure of the RNA helicase MLE reveals the molecular mechanisms for uridine specificity and RNA-ATP coupling. *Mol. Cell* **60**, 487–499 https://doi.org/10.1016/j.molcel.2015.10.011

51 Polach, K.J. and Uhlenbeck, O.C. (2002) Cooperative binding of ATP and RNA substrates to the DEAD/H protein DbpA. *Biochemistry* **41**, 3693–3702 https://doi.org/10.1021/bi012062n

52 Kim, S.H., Smith, J., Claude, A. and Lin, R.J. (1992) The purified yeast Pre-messenger-Rna splicing factor Prp2 is an Rna-Dependent Ntpase. *EMBO J.* **11**, 2319–2326

53 Moore, K.J.M. and Lohman, T.M. (1994) Kinetic mechanism of adenine-nucleotide binding to and hydrolysis by the *Escherichia coli* rep monomer. 1. Use of fluorescent nucleotide analogs. *Biochemistry* **33**, 14550–14564 https://doi.org/10.1021/Bi00252a023
54 Schutz, P., Wahlberg, E., Karlberg, T., Hammarstrom, M., Collins, R., Flores, A. et al. (2010) Crystal structure of human RNA helicase A (DHX9): structural basis for unselective nucleotide base binding in a DEAD-box variant protein. *J. Mol. Biol.* **400**, 768–782 https://doi.org/10.1016/j.jmb.2010.05.046
55 Chen, W.F., Rety, S., Guo, H.L., Dai, Y.X., Wu, W.Q., Liu, N.N. et al. (2018) Molecular mechanistic insights into drosophila DHX36-mediated G-quadruplex unfolding: a structure-based model. *Structure* **26**, 403–415.e4 https://doi.org/10.1016/j.str.2018.01.008
56 Tauchert, M.J., Fourmann, J.B., Christian, H., Luhrmann, R. and Ficner, R. (2016) Structural and functional analysis of the RNA helicase Prp43 from the thermophilic eukaryote *Chaetomium thermophilum*. *Acta Crystallogr. F Struct. Biol. Commun.* **72**, 112–120 https://doi.org/10.1107/S2053230X15024498
57 Appleby, T.C., Anderson, R., Fedorova, O., Pyle, A.M., Wang, R., Liu, X.H. et al. (2011) Visualizing ATP-dependent RNA translocation by the NS3 helicase from HCV. *J. Mol. Biol.* **405**, 1139–1153 https://doi.org/10.1016/j.jmb.2010.11.034
58 Luo, D.H., Xu, T., Watson, R.P., Scherer-Becker, D., Sampath, A., Jahnke, W. et al. (2008) Insights into RNA unwinding and ATP hydrolysis by the flavivirus NS3 protein. *EMBO J.* **27**, 3209–3219 https://doi.org/10.1038/emboj.2008.232
59 Schwer, B. (2008) A conformational rearrangement in the spliceosome sets the stage for prp22-dependent mRNA release. *Mol. Cell* **30**, 743–754 https://doi.org/10.1016/j.molcel.2008.05.003
60 Jain, R., Coloma, J., Garcia-Sastre, A. and Aggarwal, A.K. (2016) Structure of the NS3 helicase from Zika virus. *Nat. Struct. Mol. Biol.* **23**, 752–754 https://doi.org/10.1038/nsmb.3258
61 Taylor, L.L., Jackson, R.N., Rexhepaj, M., King, A.K., Lott, L.K., van Hoof, A. et al. (2014) The Mtr4 ratchet helix and arch domain both function to promote RNA unwinding. *Nucleic Acids Res.* **42**, 13861–13872 https://doi.org/10.1093/nar/gku1208
62 Buttner, K., Nehring, S. and Hopfner, K.P. (2007) Structural basis for DNA duplex separation by a superfamily-2 helicase. *Nat. Struct. Mol. Biol.* **14**, 647–652 https://doi.org/10.1038/nsmb1246
63 Ledoux, S. and Guthrie, C. (2016) Retinitis pigmentosa mutations in bad response to refrigeration 2 (Brr2) impair ATPase and helicase activity. *J. Biol. Chem.* **291**, 11954–11965 https://doi.org/10.1074/jbc.M115.710848